Narasipura *et al.*
Journal of Neuroinflammation (2025) 22:36
https://doi.org/10.1186/s12974-025-03353-2

Journal of Neuroinflammation

RESEARCH

Open Access

Inflammatory responses revealed through HIV infection of microglia-containing cerebral organoids

Srinivas D. Narasipura[1†], Janet P. Zayas[1†], Michelle K. Ash[1], Anjelica F. Reyes[1], Tanner Shull[1], Stephanie Gambut[1], James L. A. Szczerkowski[1], Charia McKee[1], Jeffrey R. Schneider[1], Ramon Lorenzo-Redondo[2,3], Lena Al-Harthi[1*] and João I. Mamede[1*]

Abstract

Cerebral organoids (COs) are valuable tools for studying the intricate interplay between glial cells and neurons in brain development and disease, including HIV-associated neuroinflammation. We developed a novel approach to generate microglia containing COs (CO-iMs) by co-culturing hematopoietic progenitors and inducing pluripotent stem cells. This approach allowed for the differentiation of microglia within the organoids concomitantly with the neuronal progenitors. Compared with conventional COs, CO-iMs were more efficient at generating $CD45^+/CD11b^+/Iba\text{-}1^+$ microglia and presented a physiologically relevant proportion of microglia (~ 7%). CO-iMs presented substantially increased expression of microglial homeostatic and sensome markers as well as markers for the complement cascade. CO-iMs are susceptible to HIV infection, resulting in a significant increase in several pro-inflammatory cytokines/chemokines, which are abrogated by the addition of antiretrovirals. Thus, CO-iM is a robust model for deciphering neuropathogenesis, neuroinflammation, and viral infections of brain cells in a 3D culture system.

Keywords Cerebral organoids, Microglia, HIV, Neuropathogenesis, Neuroinflammation, IPSC, HPC

Introduction

Neurodegenerative diseases are debilitating disorders characterized by deterioration of brain function and affect millions of people worldwide. Currently, the most utilized models for studying brain diseases involve *post-mortem* human brain tissue [1, 2], non-human primates (NHPs) [3], small animal models [4–7], and in vitro 2-dimensional (2D) cultures of primary cells (mostly fetal in origin) [8] or cell lines [9–12]. While relevant in the context of their specific studies, many of these models are limited by availability, cost, and differences between species [5, 13]. Cerebral organoids have emerged as tools for studying the health and disease of the human brain [14, 15]. COs provide a three-dimensional (3D) architecture of resident brain cells (neurons, astrocytes, oligodendrocytes, and microglia), although they lack vascularization of the tissue environment. They are developed from embryonic stem cells (ESCs) or induced pluripotent stem cells (iPSCs) to form 3D tissue organization and spatial arrangements of diverse CNS cell types that recapitulate the intricate pattern and functionality of brain tissue

†Srinivas D. Narasipura and Janet P. Zayas are contribute equally to this work.

*Correspondence:
Lena Al-Harthi
lena_al-harthi@rush.edu
João I. Mamede
joao_mamede@rush.edu
[1] Department of Microbial Pathogens and Immunity, Rush University Medical Center, Chicago, IL, USA
[2] Department of Medicine, Division of Infectious Diseases, Northwestern University Feinberg School of Medicine, Chicago, IL, USA
[3] Center for Pathogen Genomics and Microbial Evolution, Institute for Global Health, Northwestern University Feinberg School of Medicine, Chicago, IL, USA

[16–19]. Organoids of various parts of the brain, such as the forebrain, midbrain, and hippocampus, are powerful tools for studying neurodegenerative diseases, neurodevelopmental disorders, and the interplay between brain cells under homeostatic and diseased conditions [20]. As the genetic manipulation of iPSCs is very well established, COs allow the study of specific molecular mechanisms related to brain biology and neurovirology. Furthermore, COs express genes associated with human cortical development, and developing neurons display active neural networks [21, 22].

Despite their progress as a powerful model platform to study neuronal diseases at the organ level, COs lack a proper abundance of cell types that are of non-ectodermal origin, such as microglia [23]. To circumvent this, short-term co-cultures of pre-differentiated microglia are engrafted into organoids; however, the extent to which these incorporated microglia survive and function in these structures is unknown [24–27].

Human immunodeficiency virus (HIV) can invade the brain as early as 8 days post-infection [28–30], initiating an inflammatory cascade leading to neuronal injury that clinically manifests as HIV-associated neurocognitive disorders (HAND). Close to 50% of people living with HIV (PLWH) suffer from HAND [31, 32], a spectrum of neurocognitive impairments that range from mild cognitive and motor impairments to severe dementia. HAND can significantly affect the quality of life and daily functioning of those impacted [30, 33]. While the mechanisms driving HAND are multifaceted, low levels of HIV in the brain under antiretroviral therapy (ART) contribute to persistent neuroinflammation [34, 35]. There is evidence of pockets of replication in peripheral tissues despite suppressive ART, where the presence of low levels of viral RNA, DNA, and proteins is thought to be the primary driver of neuroinflammation [33, 36–39].

There are numerous models used to study HIV neuropathogenesis, each with its own limitations. While human samples are ideal for studying HIV in the brain, *post-mortem* samples of the brain are often difficult to obtain, and these cohorts are usually heterogeneous in terms of their treatment regimens and comorbidities, as well as the method of preservation utilized during brain collection. Longitudinal assessment of brain tissue from PLWH is also difficult. Nonhuman primates serve as important models of HIV/SIV neuropathogenesis; however, SIVmac and SHIVs are not genetically identical to HIV-1, and there are profound differences in species-specific responses, including differential molecular aspects of viral replication, disease progression and responses [40, 41]. While humanized mouse models have human immune cells, a vast majority of host cells in the brain are resistant to HIV infection [42]. These studies are also conducted in the backdrop of graft versus host disease (GVHD) [43], which develops in all humanized models and has to be controlled for [42, 44]. These caveats to existing models for studying HIV in the brain underscore the need to develop models of brain cells in 3D culture systems that recapitulate the human condition.

Microglia, the resident myeloid cells of the brain, are the major cell type infected by HIV in the CNS [45, 46]. Astrocytes, the most abundant glial cells in the brain, are infected to a lesser extent and have mechanisms to suppress HIV transcription [47–50]. Macrophages and infiltrating T cells are also known to harbor HIV in the brain [51–53]. The development of appropriate models to dissect the role of microglia in HIV infection is paramount not only for understanding HIV-associated neuroinflammation but also for studying the brain as a reservoir for HIV. This brain reservoir contributes to the overall reservoir of HIV in the body, as HIV can egress from the brain to seed other lymphoid tissues [54]. Recently, Tang et al. reported that microglia isolated from the adult human brain are susceptible to HIV infection and lack significant viral genetic diversity, indicating that the microglial reservoir is seeded early in infection [55]. However, these studies exploit monolayer cell cultures of microglia in the absence of other cell types. Using innately developed microglia in a CO model, Ormel et al. demonstrated HIV-1 infection of microglia [56]. Recent experiments using polybrene, along with spinoculation, have shown high infection levels of microglia with lower amounts of HIV [57]. The limitations of this model include the presence of fewer microglia ($\leq$2%) than in the human brain, which could make it extremely difficult to dissect the mechanisms of viral infection and replication in microglia. Microglia isolated from these organoid models exhibited successful infection by HIV, albeit at a poor rate [58]. dos Reis et al. engrafted infected microglia (adult primary or a cell line) into COs [59]. While this method is adequate for incorporating microglia into COs, it has several drawbacks, as the microglia engrafted into COs are previously infected rather than infected after incorporation into the tissue environment, and the study uses cell cultures that are difficult to obtain for large-scale experiments. Furthermore, using ESCs overexpressing the PU.1 transcription factor or co-culturing hiPSC-derived neuronal precursor cells (NPCs) with primitive macrophage progenitors (PMPs) resulted in organoid generation with controllable proportions of human microglia (8–10%) in COs [60–62]. However, the goal of these studies was not to study HIV infection.

Recently, in an elegant study by Schafer et al. xenotransplanted erythromyeloid progenitors incorporated COs into the adult NOD/SCID mouse brain and generated functionally mature human microglia that can operate

within a physiologically relevant vascularized brain environment [63]. Although this model can provide excellent insights into the biology and pathology of human microglia, laborious surgical methods make large-scale studies impractical. Furthermore, complications in the study of HIV pathogenesis may arise from the resistance of the mouse immune system to HIV infection and the rapid occurrence of GVDH to humanization.

Hematopoietic progenitors (HPCs), also known as erythromyeloid progenitors (EMPs), derived from iPSCs differentiate into microglia when properly cued [64]. Using this principle, we developed an approach to generate COs containing microglia by combining HPCs with iPSCs during the first stage of embryoid body formation. We demonstrated the successful proliferation, differentiation, and maturation of HPCs incorporated into microglia in mature COs. These cerebral organoids containing microglia (CO-iMs) express high levels of microglia-specific homeostatic and sensome markers. They were successfully infected with HIV and exhibited augmented neuroinflammatory characteristics with infection. Furthermore, by incorporating constitutively expressed red fluorescent protein (RFP) into HPCs, we demonstrated that microglia in CO-iMs are specifically amenable to genetic modifications.

Results

Microglia are efficiently differentiated in organoids produced by combining iPSCs with HPCs during EB formation

Given that HPCs (or erythromyeloid progenitor cells, EMPs), when provided with proper cues, can differentiate into microglia in vitro [65], we hypothesized that mixing HPCs with iPSCs during the EB formation stage and providing appropriate conditions (MCSF and IL-3) allows HPCs to proliferate and differentiate into microglia in line with organoid maturation. We first confirmed iPSC lines to be of high quality by morphology (colonies with tight borders with less than 5% differentiation, Suppl. Figure 1A) and by phenotype (the expression of the classical markers OCT-4 and TRA-1–60 pluripotency markers and the Ki-67 proliferation marker in more than 95% of the cells; Suppl. Figure 1B). We then differentiated unlabeled, or RFP-labeled, iPSCs into HPCs and confirmed their small spherical floating cell morphology (Suppl. Figure 1C) and the expression of the key progenitor marker CD43 (>80% of cells), the stemness marker CD34 (~60% of cells) and the myeloid marker CD45 (Suppl. Figures 1D and E). In addition, efficient labeling of iPSCs and HPCs derived from this iPSC-Ru line with constitutively expressing turboRFP was also confirmed (Suppl. Figures 1F–I). Next, we generated unguided cerebral organoids (COs) and generated CO-iMs by mixing iPSCs with HPCs at a 10:3 ratio on day 0 and incubated both types of organoids with MCSF (50 ng/ml) and IL-3 (20 U/ml) throughout the formation, expansion and maturation stages. The schematic in Fig. 1A outlines both approaches. We did not observe any changes in the morphological features, including the measured size of CO-iMs at any developmental stage when HPCs were incorporated compared with COs (Fig. 1B, C). Cyclic multiplex immunofluorescence (mIF) imaging of approximately 60- to 70-day-old CO-iMs revealed the robust presence of TMEM119$^+$ and Iba1$^+$ microglia (Fig. 1D–F and Suppl. Figures 2A–D). Furthermore, mIF confirmed the robust presence of astrocytes (GFAP$^+$/S100β$^+$) and neurons (Tuj1$^{+/}$NeuN$^+$) in CO-iMs. Additional lineage-specific markers for glial and neuronal cells were also used, which revealed the presence of differential marker expression in these cell types; for example, not all GFAP$^+$ cells were S100β$^+$. Similarly, not all NeuN$^+$ cells were Tuj1$^+$ or MAP2$^+$ (Fig. 1D–F and Suppl. Figures 2A–D). We quantified astrocytic (GFAP$^+$ and S100β$^+$), neuronal (Tuj1$^+$) or NPC (Nestin$^+$) populations in these organoids via flow cytometry (Suppl. Figures 2E–H). The incorporation of HPCs did not affect the relative proportions of NPCs (~30–37%, Nestin$^+$), astrocytes (~38–40%, S100β$^+$ and ~45–55%, GFAP$^+$), or neuronal cells (~45–50%, Tuj1$^+$) between COs and CO-iMs (Suppl. Figures 2I and J). However, there was a significant increase (~4.6-fold) in myeloid (CD45$^+$) cells in CO-iMs compared with COs (Fig. 2A, B). In line with these findings, we observed a significant increase (~3.5–fourfold) in the number of CD11b/Iba1 double-positive cells (Fig. 2C). As expected, CD11b/Iba1 double-positive cells were found only in the CD45$^+$ population and were devoid in CD45$^-$ population (Fig. 2A, bottom dot plots). Interestingly, within the CD45$^+$ myeloid population, there were

(See figure on next page.)

Fig. 1 Generation and characterization of CO-iMs generated from iPSC-Ru. **A** Schematic flow diagram indicating the timeline as well as all developmental stages for generation of COs and CO-iMs. **B** Representative bright field images of a CO and a CO-iM through different stages of their development. Scale bars, 100 µm. **C** Diameter sizes of COs and CO-iMs measured at key time points during their differentiation (n = 5 per time point). **D** Left, representative multiplex IF image of a CO-iM stained for nucleus (Hoechst, white), microglia (TMEM119, red), neurons (green, Tuj1) and astrocytes (GFAP, blue). Scale bar, 100 µm. Panel on the right showing individual staining for indicated markers and a merged image from all. Scale bars, 500 µm. **E**, **F** Zoomed insets of i), and ii) regions in (**D**). Scale bars, 100 µm

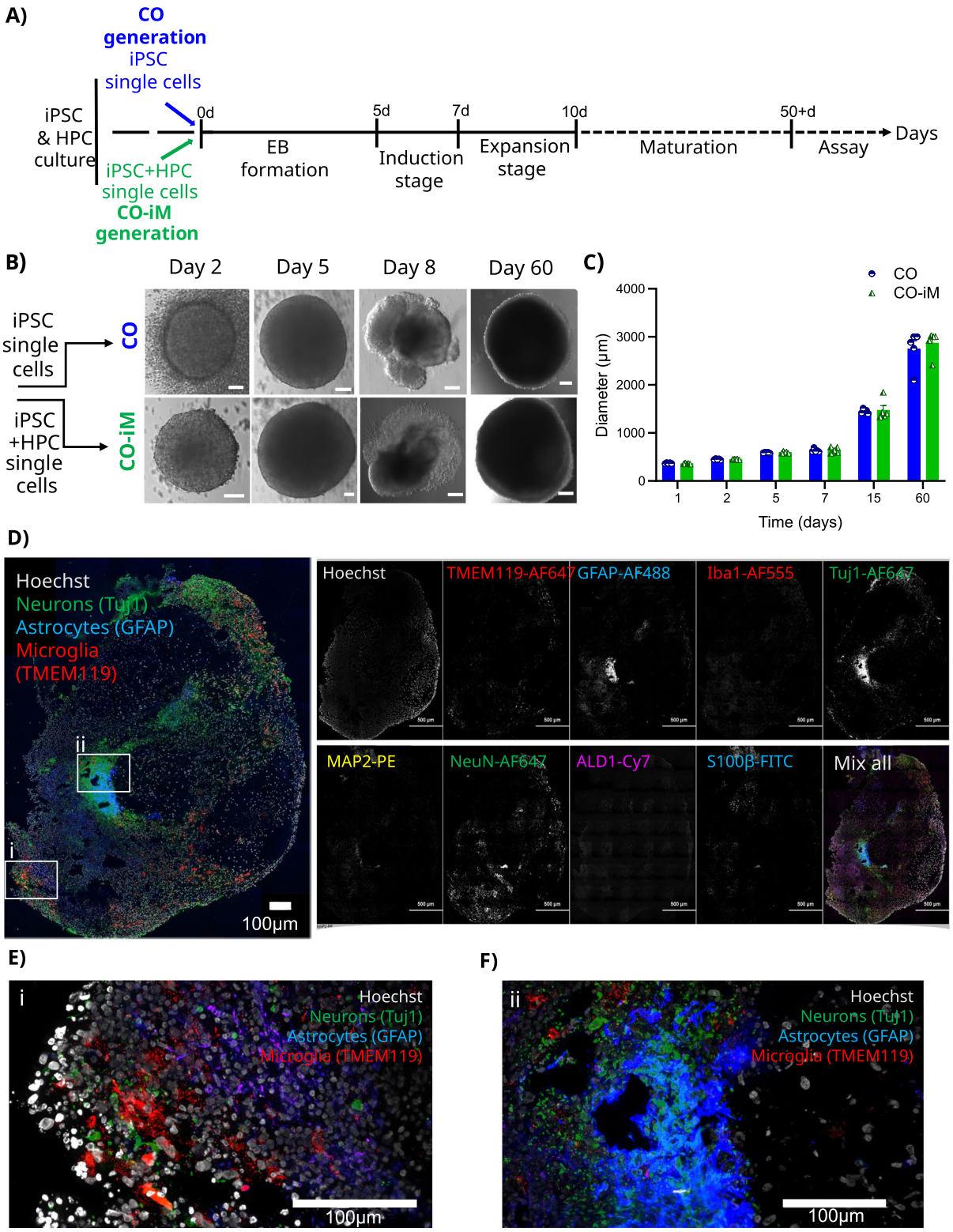

Fig. 1 (See legend on previous page.)

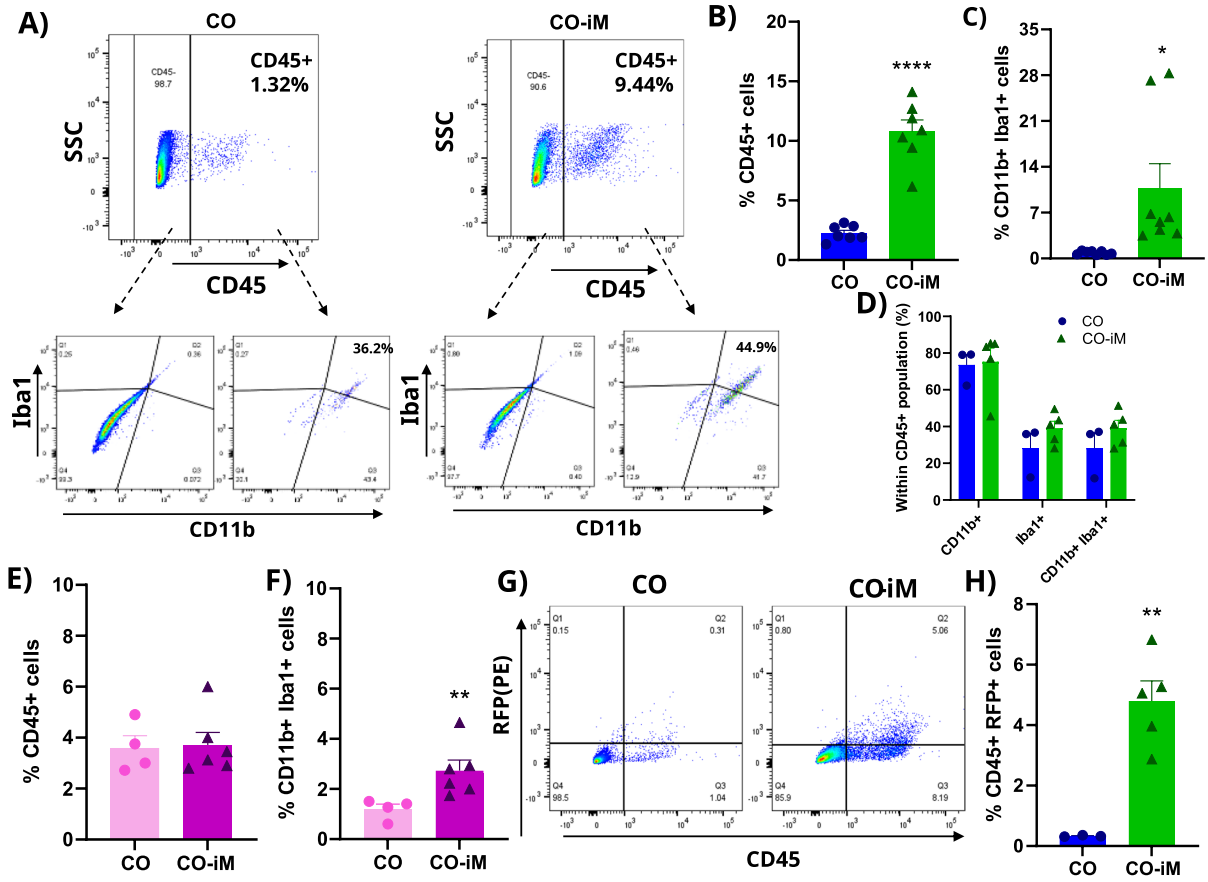

Fig. 2 Phenotypic characterization reflecting enrichment of microglia in CO-iMs. COs and CO-iMs were processed and dissociated into single cell suspension, stained, and analyzed for cell surface and intracellular proteins by flow cytometry. **A** Representative dot plots showing $CD45^+$ and $CD45^-$ populations from total cells (top), and $CD11b^+$ and $Iba1^+$ populations (bottom) in organoids generated from iPSC-Ru line. Arrows indicate populations analyzed within $CD45^+$ or $CD45^-$ gates. **B, C** Cumulative data indicating percent $CD45^+$ and CD11b /Iba1 double positive cells in total population of organoids generated using iPSC-Ru line (n = 7–8 represents COs and CO-iMs, from two independent respective batches). **D** Cumulative data showing percent CD11b/Iba1 single positive as well as double positive cells within $CD45^+$ population in organoids generated using iPSC-Ru line (n = 3 for COs, and n = 5 for CO-iMs, from respective single batches). **E**, **F** Cumulative data showing percent CD45 single positive as well as CD11b/Iba1 double positive cells within $CD45^+$ population in organoids generated using iPSC-CRL line (n = 4 for COs, and n = 6 for CO-iMs, from respective single batches). **G** Representative dot plots showing that the majority of RFP^+ cells are also $CD45^+$ cells in CO-iMs from iPSC-Ru. **H** Cumulative data indicating percent RFP^+ $CD45^+$ population (n = 3 for COs, and n = 5 for CO-iMs from iPSC-Ru, from respective single batches). Each symbol represents an individual organoid. Data are presented as mean ± SEM using non-parametric Mann-Whitney test. *p < 0.05, **p < 0.01, ***p < 0.001.

similar proportions of CD11b/Iba1 single-positive or double-positive cells in both COs and CO-iMs (Fig. 2D). Further, flow analysis on ~ 65-day old CO-iMs, showed a small fraction (< 2%) of cells to be positive for CD3, a marker of T cells (Suppl. Figure 2 K). In parallel, in the organoids generated via iPSC-CRL, although there was no difference in the $CD45^+$ population, there was a significantly higher (~ twofold) proportion of CD11b/Iba1 double-positive cells in CO-iMs when compared to COs (Fig. 2E, F). In addition, in CO-iMs generated with HPCs stably expressing RFP, most RFP^+ cells were $CD45^+$ (> 6%, Fig. 2G, H). As previously reported, we detected a $CD45^+/Iba1^+$ microglia population in COs, albeit at lower levels (Fig. 2B, C, F and H) [56]. Taken together, these results demonstrate that HPCs incorporated at the beginning of EB formation successfully proliferate and differentiate into mature microglia in the same timeframe as the overall growth and maturation of the neurons and astrocytes in the brain organoids.

Transcription analysis exhibit induced expression of key microglia-specific genes in CO-iMs

To further characterize the myeloid cells in CO-iMs for proliferation, abundance, differentiation and maturation,

we quantified the transcriptional profiles of important homeostatic microglial markers, such as *CD11B*, *IBA1* and *TMEM119* [66], along with *CD45*, a myeloid marker expressed at lower levels than monocytes/macrophages in steady-state microglia [67]. We found that the expression levels of all these specific genes were significantly greater in CO-iMs than in conventional COs. The trend was similar when the data were normalized to either *GAPDH* (Fig. 3A) or *18S* endogenous controls (Suppl. Figure 3A). Interestingly, in CO-iMs, the level of *CD45* induction was much lower than that of *CD11B* or *IBA1* induction (~8–10-fold vs 60–100-fold; Fig. 3A), suggesting that low expression of *CD45* in combination with high *CD11B* expression may indicate a resting steady-state feature of microglia in CO-iMs [67, 68]. The expression levels of astrocyte markers (*S100β, ACSBG1* and *EAAT1*), neuronal progenitor/immature neuron markers (*Vimentin* and *Nestin*) and mature neuronal markers (*MAP2* and *NEUN*) were similar between CO-iMs and COs (Fig. 3B–D and Suppl. Figure 3B). Furthermore,

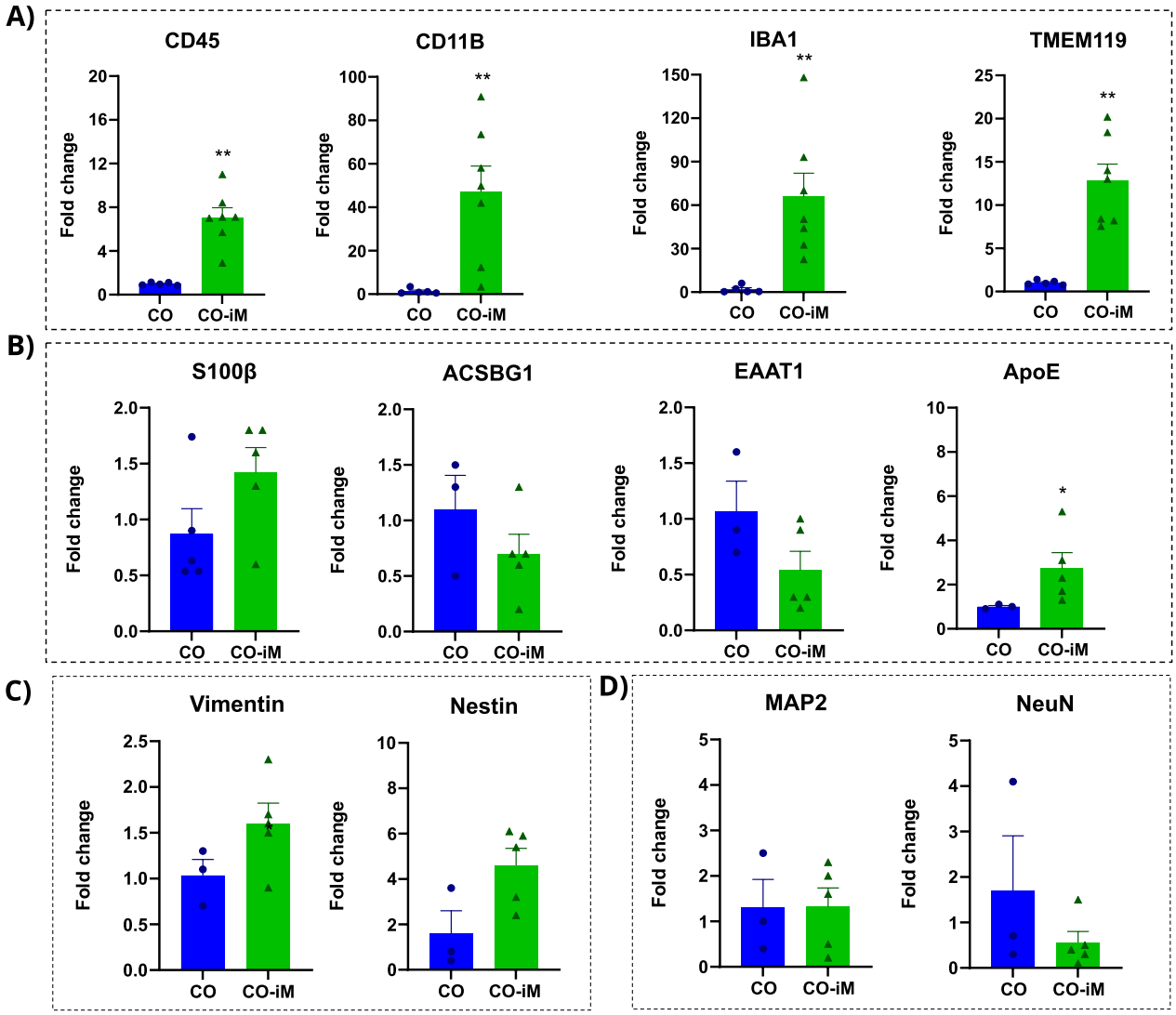

Fig. 3 Genotypic characterization reflecting enrichment of microglia markers in CO-iMs. RT-qPCR analysis of COs and CO-iMs generated from iPSC-Ru**.** mRNA levels were normalized to the endogenous reference *GAPDH* and expressed as fold change relative to CO using the $2^{-(\Delta\Delta Ct)}$ method. Fold change for each sample in COs was assessed by subtracting its delta Ct from average delta Ct, followed by $2^{-(\Delta\Delta Ct)}$. **A** mRNA levels of homeostatic microglia markers: *CD45*, *CD11B*, *IBA1* and *TMEM119* (n = 5 for COs from one batch; n = 7 for CO-iMs from two batches). **B** mRNA levels of astrocyte markers: *S100β*, *ACSBG1*, *EAAT1* and *APOE* (n = 3–5 from respective single batches). **C, D** mRNA levels of neuronal progenitor and mature neuronal markers: *Vimentin, Nestin*, *MAP2* and *NeuN*. Each symbol represents an individual organoid from respective single batches. Data are presented as mean ± SEM using non-parametric Mann–Whitney test. *p < 0.05, **p < 0.01, ***p < 0.001

the transcription level of *APOE*, a lipid transporter that is expressed mainly in astrocytes, was slightly greater in CO-iMs than in COs. Statistical analysis suggested that normalization to *GAPDH* was significant and that normalization to *18S* reference controls was not significant (Fig. 3B and Suppl. Figure 3B).

Similar observations with respect to gene expression were noted in organoids generated from the iPSC-CRL line. The expression of *CD11B* and *IBA1* was significantly greater in CO-iMs than in COs (Suppl. Figures 3C and D). *S100β* and *Nestin* levels were not different between COs and CO-iMs (Suppl. Figure 3E and F). Surprisingly, the expression levels of *CD45* mRNA and *TMEM119* mRNAs were not significantly different between COs and CO-iMs with this iPSC line (Suppl. Figures 3C and D), as was the case for CD45 protein expression (Fig. 2E). These findings reflect inherent intra- and inter-group variations, as observed among batches and different iPSC cell lines [18, 22, 69].

To assess the differences between COs and CO-iMs in depth, we characterized the global transcriptome profile and compared COs and CO-iMs via RNA-seq analysis. Gene enrichment analysis of the differentially expressed genes revealed striking differences in genes involved in immunity, such as phagocytosis, leukocyte migration, chemotaxis, and cell migration (Fig. 4A), and pathways such as complement and coagulation, interactions of cytokine receptors with cytokines and foreign antigens, and TLR signaling (Fig. 4B). Differential gene expression (DGE) analysis revealed 1,412 (5.6% of the total number of genes tested) genes that were significantly upregulated in CO-iMs compared with COs (FDR < 0.05 and log2-fold change > 1) and 1,486 (5.9% of the total tested) downregulated genes, indicating significant changes associated with the inclusion of microglia in the COs (Fig. 4C and Suppl. Dataset 1). We subsequently performed a gene set enrichment analysis (GSEA) with the entire list of quantified genes ranked by the log2-fold change in the CO-iM vs CO comparison. We observed a significant enrichment of genes related to complement, cytokine expression, and innate immunity (Fig. 4A, B) among the genes upregulated in CO-iMs compared with COs (Fig. 4C). Among the downregulated genes, genes related to neuronal and astrocytic homeostatic functions were enriched. Interestingly, we found that genes with important brain functions, such as *CDA* and *PKD2L1*, which have BBB and oligodendrocyte myelination functions, respectively, were significantly upregulated in CO-iMs. Conversely, *LINGO4*, a gene anticipated to operate either upstream or within the positive regulation of synapse assembly, is downregulated, which might point to important microglial molecular functions in synapse regulation, as reviewed previously [70].

Microglia sense changes in their surroundings for immune regulation and host defense functions. Therefore, we quantified the expression of the microglia-specific sensome genes listed from a well-established cluster [71, 72]. Heatmap analysis revealed significant enrichment of the majority of these genes in CO-iMs compared with COs (Fig. 4D). Validation by RT-qPCR analysis revealed significant induction of the expression of some of these genes such as *TLR4*, *CSF1-R* and *TMEM119*, together with a trend toward induction of *CX3CR1* and *SLCO2B1* in CO-iMs compared with COs, except for

(See figure on next page.)

Fig. 4 Transcriptional Profile of COs and CO-iMs. RNA-seq analysis of ~65-day old iPSC-Ru line derived COs (n = 3) and CO-iMs (n = 3) from respective single batches. **A** Dot plot showing the enriched GO terms of biological processes and molecular functions amongst activated and suppressed genes identified using absolute log2 fold change > 1 and a false discovery rate (FDR) < 0.05 using the Benjamin-Hochberg procedure in CO-iMs when compared to COs. **B** Dot plot showing the enriched REACTOME pathways (FDR < 0.1) in activated as well as suppressed genes in CO-iMs when compared to COs. For (**A**, **B**) the x-axis indicates the ratio of genes identified by our analysis and the total number of genes that constitute the pathway, the size of the dot is based on gene count in the pathway, and the color of the dot shows the pathway enrichment significance. **C** Volcano plot comparison of CO-iMs vs COs indicating average log2 (fold change) versus –log10 (FDR) for all genes. Genes upregulated and downregulated by 2-fold change and FDR < 0.05 are labeled with red dots. **D** A heatmap showing expression of microglia sensome markers in individual replicates of CO-iMs and COs, (n = 3 for CO-iMs and COs). Color indicates the expression level scaled for each gene by centering and scaling. **E** RT-qPCR quantification to determine mRNA levels of microglia immune sensome markers: *CX3CR1*, *SLCO2B1*, *TLR4*, *CSF1-R* and *P2RY12*. **F** RT-qPCR quantification to determine mRNA levels of *IL34*, an essential cytokine for microglia maturation and survival. **G** RT-qPCR quantification to determine mRNA levels of *C3* and *C1Q*, components of complement pathway. **H** Heatmap showing expression of microglia complement pathway genes in individual replicates of CO-iMs and COs, (n = 3 for CO-iMs and COs). Color indicates the expression level scaled for each gene. **I** Uniform Manifold Approximation and Projection (UMAP) plot for dimension reduction of 11,440 barcoded single cells derived from 4 individual CO-iMs (~120 day old) subjected to scRNA seq analysis exhibiting 12 distinct clusters as identified by graph-based clustering of cell-specific gene expression. Subsequent cell annotation allowed us to define the most likely cell type corresponding to each cluster. The bubble plot shows all the cell types that were considered by ScType for cluster annotation that were assigned to at least 100 cells with the exception of cluster 10 where no assignment reached that cut-off, and the only assignment obtained is shown. The outer bubbles correspond to each cluster with size reflecting the number of cells in the cluster, while the inner bubbles correspond to considered cell types for each cluster, with the biggest bubble corresponding to assigned cell type, except for cluster 3 and 10 where we did not obtain high quality assignments

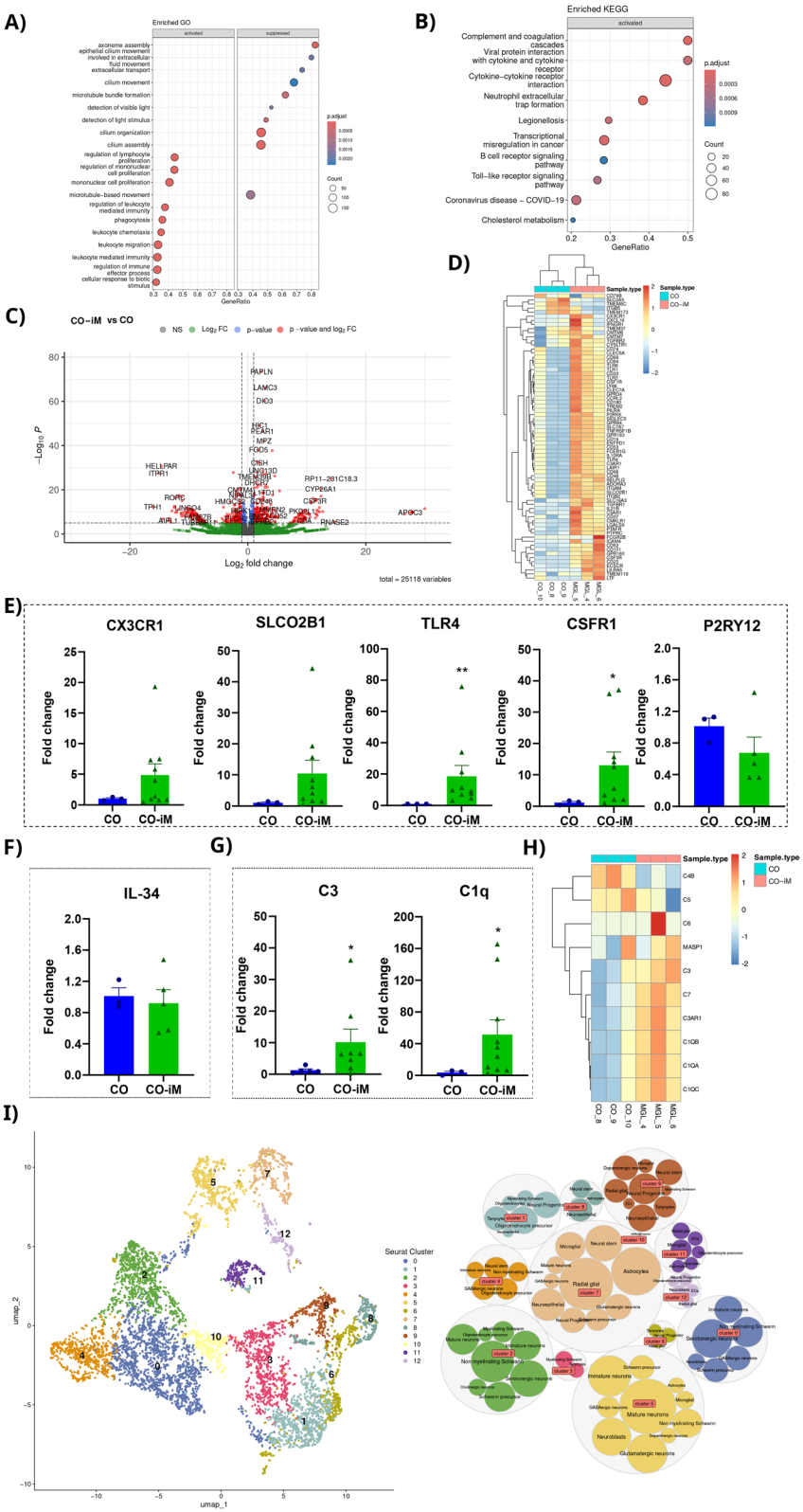

Fig. 4 (See legend on previous page.)

P2RY12, whose expression was unchanged between CO-iMs and COs (Figs. 3A, 4E and Suppl. Figures 3A). MCSF and IL34 are required for the survival, proliferation, and maturation of microglia [67, 68]. CSF1-R is the common receptor for MCSF and IL34. We provided MCSF along with IL-3 throughout the culture period. Substantial induction of *CSF1-R* mRNA in CO-iMs (Fig. 4E and Suppl. Figure 4A), along with similar yet noticeable levels of *IL34* mRNA in both types of organoids (Fig. 4F and Suppl. Figure 4B) indicated a self-sufficient milieu, not only for initial proliferation and differentiation of HPCs into microglia but also for survival, proliferation, and maturation of microglia in our 60 + day-old, cultured organoids. Microglia play an important role in synapse pruning (removal of excess and less active synapses) via the classical complement pathway in the developing brain. Synapse pruning is pivotal in the maintenance and refinement of synapses [73]. We assessed the expression levels of *C1Q* and *C3*, two early key players in complement pathways, via qPCR. These two mRNAs were significantly elevated in CO-iMs (Fig. 4G and Suppl. Figure 4C). Similar observations were made in CO-iMs generated from iPSC-CRLs, with the exception of *C1Q*, which did not differ between the two types of organoids (Suppl. Figure 4D). In addition to *C3*, the heatmap analysis indicated the induction of additional members of complement pathways, including *C7*, *C3AR1* and *MASP1,* in CO-iMs (Fig. 4H). Receptor C3AR1 binds with C3a to activate chemotaxis. C7 initiates membrane attack complex (MAC) formation by binding with C5b-C6 along with MASP1 as a part of the terminal complement pathway. While *C6* was unchanged between CO and CO-iMs, *C5* and *C4B* were significantly downregulated in CO-iMs (Fig. 4H). Cleavage of C5 results in C5a and C5b. C5a is an anaphylatoxin with potent spasmogenic and chemotactic activity while C5b acts as a subunit of the MAC. C4b complexes with C2b to form C3 convertase and activates classical complement cascade. These results suggest homeostatic maintenance of the complement cascade. Collectively, these results demonstrate that microglia generated in CO-iMs exhibit adult-like features, including the expression of homeostatic and immune surveillance genes.

While targeted approaches and bulk RNA-seq capture the overall trends of CO-iMs and mIF can capture different expression profiles and different spatial cellular distributions, they are less powerful in detecting unknown or less abundant cell types and subtypes. Thus, to capture the molecular identity of different cell types more accurately, we isolated single cells from four CO-iMs (approximately 4 months old), pooled them into 2 groups and performed scRNA-seq on a total of 13,000 cells. Graph-based cell clustering based on transcriptional patterns revealed 13 distinct clusters that we could assign to 11 main CNS cell types (Fig. 4I), as indicated by the larger bubbles within each cluster in Fig. 4I, including various types of neurons such as mature, serotonergic and others (mainly in clusters 0 and 5, Fig 4I), microglia (in cluster 11, Fig. 4I and Suppl. Figure 3F), astrocytes (mainly in cluster 7, Fig. 4I and Suppl. Figure 3H), oligodendrocyte precursor cells, and others. Within the outer bubbles corresponding to each cluster in Fig. 4I we show the cluster's assigned cell type (represented as the biggest inner bubble per cluster) together with all cell types considered for the analysis in each cluster (smaller inner bubbles). Additionally, we confirmed these cell assignments by analyzing the most highly expressed genes in each cluster and key cell type specific markers (Suppl. Figure 3G). Taken together, the results of scRNA-seq confirmed the emergence of mature microglia in CO-iMs, confirming that the CO-iMs presented here are a good representation of different brain cells and indicating the importance of these 3D cell culture models for neural and neurovirological research where in vivo sampling is difficult.

Microglia are robustly infected with HIV in CO-iMs

As CO-iMs contain sufficient and physiologically relevant proportions of microglia, we used CO-iMs as a model to study HIV infection. Brain organoids have been previously used to model HIV, CMV and ZIKV infections [56, 59, 61, 74]. Previously, for HIV infections, mature microglia were infected first and then allowed to traffic into COs [56, 59]. Doing so will not permit the study of the complete establishment, spread, and consequences of HIV infection at different stages. Although successful HIV infection of microglia has been demonstrated in conventional COs that contain innately developed microglia [56, 57], these COs lack the physiological proportions of microglia, which may pose challenging hurdles in understanding microglia–pathogen interactions. To address the questions of the levels of microglial susceptibility to HIV and the neuropathology within an organoid to closely mimic the natural mode of infection in the CNS, CO-iMs were infected with two different infectious HIV isolates, HIV-$1_{Ba\text{-}L}$ (R5 tropic) and HIV-Gag-iGFP_JRFL [75] at 10 ng/ml of virus per organoid in low binding 24-well plates. Three days later, the wells were gently washed and replaced with fresh maturation media and two days later organoids were processed for downstream experiments. Anti-retroviral treatment consisted of nevirapine (NVP, 10 µM) and dolutegravir (DTG, 3.90 µg/mL) that were added 24 h prior to infection, at the time of infection, and after day 3 wash.

HIV infection did not affect the morphology of the organoids up to 30 days post-infection (Figs. 5A and B) [74, 76, 77]. Extracellular p24 quantification by ELISA

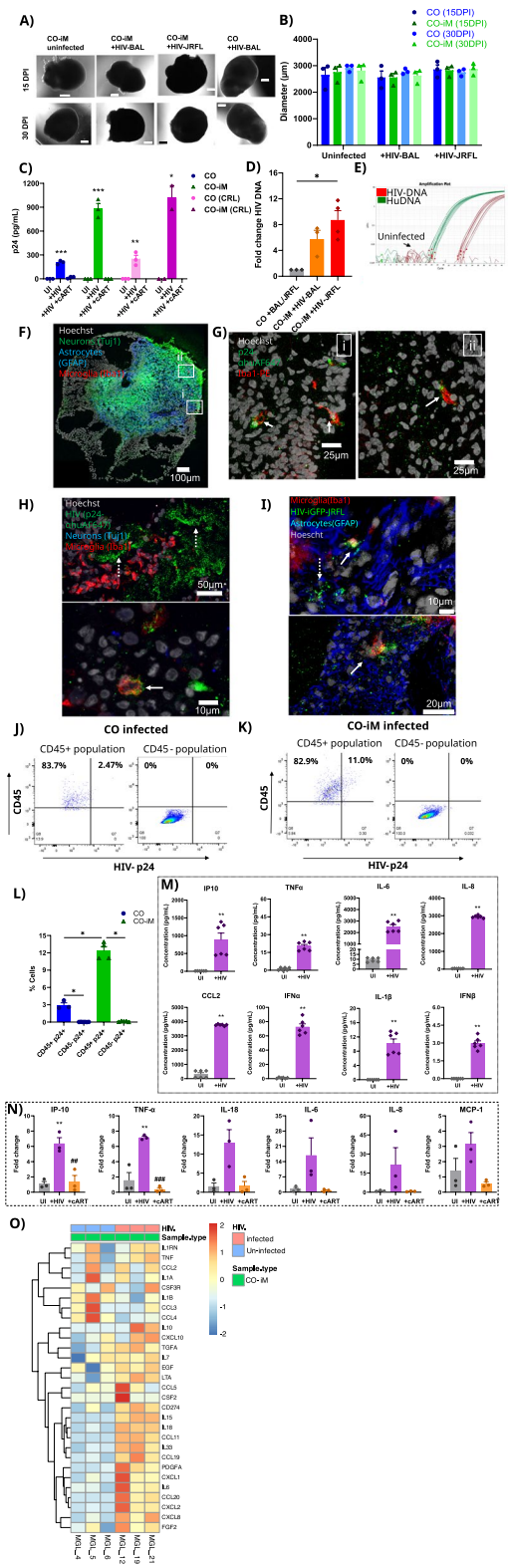

Fig. 5 Robust response of microglia to HIV-1 infection in CO-iMs. **A** Representative bright field images showing the morphology of ~ 60-day old COs and CO-iMs generated from iPSC-Ru line after 15 or 30 days post-infection (DPI) with HIV-1 or mock. Scale bars, 500 µm. **B** Diameter sizes of COs and CO-iMs from (A) measured 15 DPI or 30 DPI with HIV or mock (n = 2 for COs, and n = 3 for CO-iMs). **C** Organoids were infected with HIV_{BaL} (7 ng of p24) on day 0. At 3 DPI, organoids were washed once with PBS and replaced with fresh media. Then, at 5 DPI, the culture supernatant was collected and used to quantify p24 by ELISA. n = 3 for each condition with organoids generated from two different iPSC cell lines (iPSC-Ru and iPSC-CRL, respectively). **D** Organoids were infected with HIV_{BaL} or HIV-iGFP_JRFL as explained in (**C**), genomic DNA was extracted and quantified for HIV DNA using Taqman qPCR and represented as fold change to COs infected with HIV_{BaL} or HIV-iGFP_JRFL (n = 3 for COs, n = 3 for CO-iM + HIV_{BaL}, and n = 4 for CO-iMs + HIV-iGFP_JRFL. **E** A representative Taqman qPCR amplification plot showing amplification of human DNA as well as HIV-GAG for all samples shown in (**D**). **F** Representative mFI images of a CO-iM generated from iPSC-Ru showing $IBA1^+/HIV^+$ microglia after 5 DPI (HIV infection). Scale bars, 100 µm. **G** Zoomed in insets of regions (i) and (ii) from (**F**) showing $p24^+$ (green), $Iba1^+$ (red) cells. Scale bars, 25 µm. **H**, **I** mIF images of infected CO-iMs generated from iPSC-Ru exhibiting $p24^+$ (green) and $Iba1^+$ (red) co-expressing cells (arrows with solid lines) as well as free virus (arrows with dotted lines) nearby $Iba1^+$ cells. Scale bars, 50, 20 and 10 µm, respectively. **J, K** Organoids were infected with HIV_{BaL} for 5 days as explained, dissociated into single cell suspension and stained for cell surface (CD45) and intracellular (p24) markers for flow cytometry analysis. Representative dot plots for CD45 and p24 populations in COs (**J**, left) and in CO-iMs (**K**, right) generated from iPSC-Ru. **L** Cumulative data indicating percentage of $p24^+$ cells in $CD45^+$ and $CD45^-$ populations, respectively. n = 3 for COs, and n = 4 for CO-iMs generated from iPSC-Ru. **M** Multiplex ELISA to quantify various pro-inflammatory cytokines/chemokines in the supernatants of CO-iMs generated from iPSC-Ru, infected with HIV_{BaL} or mock for 5 days. n = 6 in each category. **N** RTqPCR analysis for mRNA expression of various pro-inflammatory cytokines/chemokines (as indicated in the figures) in CO-iMs generated from iPSC-Ru, either infected with HIV_{BaL} for 5 days, or mock infected, or infected and treated with cART. n = 3 in each category. **O** Heatmap showing relative expression of a list of inflammatory cytokines/chemokines in infected vs uninfected CO-iMs generated from iPSC-Ru (n = 3 for each group). Color indicates the expression level scaled for each gene. Each symbol represents an individual organoid from their respective CO and CO-iM single batches. Data are presented as mean ± SEM using non-parametric Mann-Whitney test. *p < 0.05, **p < 0.01, ***p < 0.001.

revealed significantly greater amounts of virus released from CO-iMs than from COs, which was completely inhibited in the presence of cART, which was used as a control for the presence of viral input in the quantified supernatants (Fig. 5C). Similarly, qPCR of these infected organoids revealed a 6-8 fold increase in HIV DNA compared with that in COs (Fig. 5D). A representative amplification plot for viral and human DNA is shown in Fig. 5E. These data demonstrate robust productive infection in CO-iMs in comparison with that in COs. Cyclic mIF analysis demonstrated co-localization of HIV

$p24^+$ (mAb staining or iGFP-Gag+) in Iba^+ microglia (Fig. 5F–I) except for the few cells that were Iba1 negative and p24+ (Fig. 5H, bottom). They could be a subset of Iba1 negative microglia [78]. An image of a whole organoid with p24 and Iba1 staining is shown in (Suppl. Figure 5A). Furthermore, we observed viral particles in regions surrounding microglia-infected cells and regions with high concentrations of viral particles surrounding microglia that are yet to be infected (arrows with dotted lines, Fig. 5H). Given our low p24 quantities of inoculum, these observations show that infected microglia productively release new viral particles. Flow cytometry-based quantification analysis indicated that HIV-iGFP+ (or $p24^+$) cells were positive for $CD45^+$, whereas the $CD45^-$ population was negative (Fig. 5J, K). We also reported significantly more $CD45^+/p24^+$ cells in CO-iMs than in COs (Fig. 5L). Furthermore, by flow cytometry, we found that the majority of HIV^+ (iGFP+) cells were $CD11b^+$, which was almost undetectable after ART treatment (Suppl. Figure 5B). Our findings demonstrate robust HIV infection in microglia, which are also the major source of productive infection in CO-iMs, fully modeling results reported from *post-mortem* brains and humanized mouse studies.

HIV infection of CO-iMs results in heightened inflammatory conditions

To determine the immunological and cellular responses to HIV infection, we examined the expression of inflammatory cytokines at the RNA and protein levels via bulk RNA sequencing, RT-qPCR, and multiplex ELISA. Multiplex ELISA revealed significantly higher secretion of several inflammatory cytokines, such as IL-6, IP-10, TNFα, IL-8, MCP1, IFNα, IL-1β and IFNβ, in the supernatants of CO-iMs infected with HIV than in those of non-infected CO-iMs (Fig. 5M). We then evaluated the mRNA expression of these cytokines under similar conditions via RT-qPCR. We found that many of these cytokine transcripts, including *IP10* and *TNFα*, were significantly induced in response to HIV infection (Fig. 5N and Suppl. Figure 5C). In parallel, heatmap analysis via RNA-seq revealed strong induction of many cytokines and chemokines, including IL-6, IP-10 and TNFα (Fig. 5O), which was abrogated by cART treatment (Fig. 5N and Suppl. Figures 5C, D). However, the levels of the *IL1β, IFNβ, and IL1α* mRNAs did not increase at the time points measured after HIV infection (Fig. 5N and Suppl. Figure 5E), their measured protein levels significantly increased (Fig. 5M), which may reflect the longstanding permanence of these cytokines in this system after transcriptional shutdown.

Transcriptome analysis between HIV-infected and non-infected CO-iMs revealed strong upregulation and activation of immune responses (IFNs signaling), *IL-10* (log2FC = 5.65), *IL-6* (log 2FC = 3.58), and *IL-33* (log2FC = 2.834) and antigen processing and presentation (Fig. 6A and B). Conversely, HIV-1 infection resulted in the suppression of pathways of glucuronidation, neuron fate commitment, neuropeptide functions, axon and forebrain development, and lipoprotein function (Fig. 6A and B). By performing DEG analysis, we identified a total of 1826 upregulated genes (7% of the total number of genes tested) (FDR < 0.05 and log2-fold change > 1) and 2158 (8.3% of the total tested) downregulated genes associated with HIV infection, indicating significant responses to infection in CO-iMs (Fig. 6C and Suppl. Dataset 2). Notably, caspase-5, a protein that is associated with pyroptosis, cell death, and inflammasome activation in response to neuronal trauma resulting in cell death [79–81], was highly upregulated with infection (log2FC = 9.26). Furthermore, DTHD1, a widely uncharacterized protein found to be involved in apoptotic events in the brain and found to be active and highly expressed in the brains of Alzheimer's disease patients and multiple sclerosis lesions [82, 83], was highly upregulated (log2FC = 23.83). In addition, other transcripts that are important for neuronal homeostasis and function, such as psynaptophysin (log2FC = −1.7), *MAP2* (log2FC = −1.77), and *EAAT2* (log2FC = −1.46), were downregulated by approximately 60–70% during infection. Strikingly, *NOS1* (log2FC = 22.34), a gene involved in nitric oxide synthesis from L-arginine, which has many neurotransmitter properties and has been shown to be related to neurotoxicity and neurodegenerative diseases, was also highly upregulated with HIV infection (Fig. 6C and Suppl. Dataset 2). Interestingly, cART treatment with and without infection only mildly reduced the expression of DEGs (< 1%, Suppl. Figure 5F and Suppl. Dataset 3).

Taken together, these data demonstrate robust infection and replication of HIV in CO-iMs, driven primarily by HIV infection of microglia in this system. Infection drives inflammatory responses in these organoids that could lead to poor neuronal health.

Discussion

We developed a microglia-containing CO model by co-culturing iPSCs and HPCs from the same lines (iPSC-Ru and iPSC-CRL) at the beginning stage of EB formation. In this 3D culture model, HPCs proliferate and mature into microglia, as indicated by robust expression of microglia-specific homeostatic markers, as well as sensory markers, in 60+ day-old organoids. In the same system and in parallel, iPSCs differentiate into NPCs, which further differentiate into mature neurons and astrocytes. Notably, by introducing HPCs at the formation stage along the 3D formation stage (expansion to maturation stage), rather than the distinct engraftment of fully differentiated

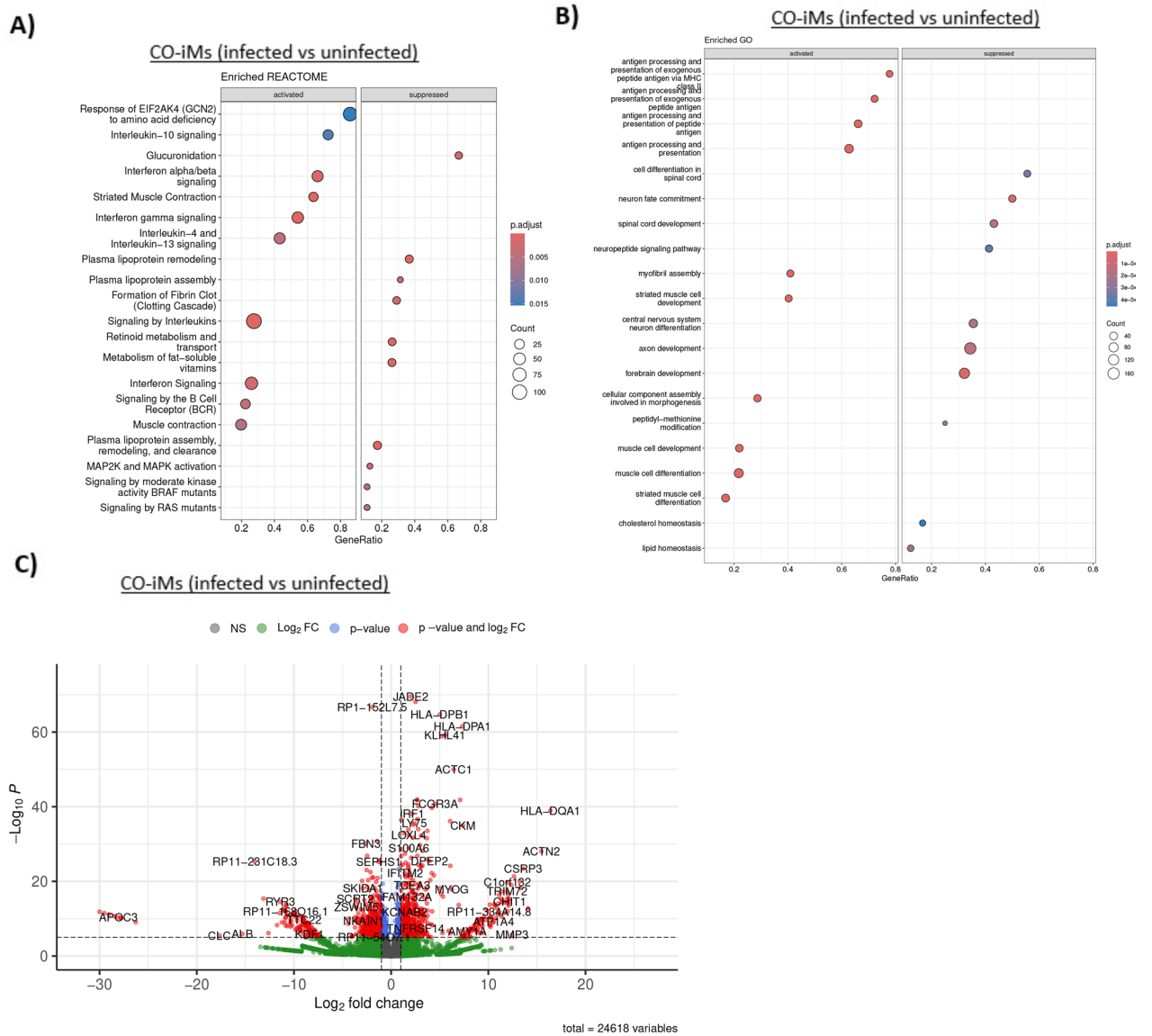

Fig. 6 Transcriptional Profiles of CO-iMs uninfected, infected with HIV, and infected + treated with cART. RNA-seq analysis of 65-day old iPSC-Ru line derived CO-iMs infected with HIV_{BaL} (n = 3) for 5 days, or mock infected (n = 3), or infected + cART treated (n = 3) for 5 days from the same production batch. **A** REACTOME dot plot showing the pathways (FDR < 0.1) enriched in activated and suppressed gene in infected CO-iMs when compared with their uninfected counterparts. **B** Dot plot showing the GO terms (FDR < 0.05) of biological processes enriched in activated and suppressed genes in infected CO-iMs when compared with their uninfected counterparts. For (**A**, **B**) the x-axis indicates the ratio of genes identified by our analysis and the total number of genes that constitute the pathway, the size of the dot is based on gene count in the pathway, and the color of the dot shows the pathway enrichment significance. **C** Volcano plot comparison of infected vs uninfected CO-iMs indicating average log2 (fold change) versus -log10 (FDR) for all genes. Genes upregulated and downregulated by two-fold change and FDR < 0.05 are labeled with red dots

microglia, we gain unique advantages, such as (i) mimicking the brain cell composition and cellular interactions from the formation of CO-iMs; (ii) using fewer HPCs/microglia per organoid, as this method does not depend on the efficiency of microglia post-engraftment; (iii) ability to regulate the number of HPCs and, in turn, microglia per organoid; and (iv) feasibility to incorporate genetically modified microglia that will differentiate from HPCs, as demonstrated by RFP^+ HPCs (Fig. 2G, H and Suppl. Figure 1F–I). Furthermore, by harnessing the self-organization capability of iPSCs instead of NPCs, we generated brain organoids (unguided type), rather than neurospheres, which can mimic the cytoarchitecture and developmental trajectories found in the neonatal brain.

Importantly, we show that microglia in our CO-iM model can be successfully and preferentially infected with HIV at a particularly high percentage, which leads to heightened inflammatory responses.

Microglia are known to account for approximately 5–10% of total cells in the CNS [84], with astrocytes and neurons being the major cell types at similar proportions, depending on the brain region and size of neurons, but typically within 20–40% [85]. In the CO-iM model, on average, approximately 7.3% of the total cells were microglia (double positive for CD11b and Iba1), whereas fewer than 1% were microglia in conventional COs (Fig. 2C). In addition, astrocytes (approximately 35–50%) and neurons (approximately 44–51%) were abundant (Fig. 2I and J), and their defining transcripts and antigens were highly expressed in CO-iM. Surprisingly, as expected, like TMEM119 (Fig. 3A), P2RY12 mRNA was not induced in CO-iMs when compared to COs, rather it was slightly yet non-significantly higher in COs (Fig. 4E). One possible explanation is that P2RY12 expression could be regulated at protein level rather than at mRNA level in microglia. Second, P2RY12 is also expressed by oligodendrocytes [86] and the proportion of these cells could be slightly higher or may have slightly induced mRNA expression in COs than in CO-iMs reflecting the observed results. Further, our scRNAseq analysis in Fig. 4I identified a cluster of clearly defined tissue-resident microglia (cluster 11) with elevated levels of markers for these cells such as TMEM119. But also, our system recapitulates various cellular subtypes such as possible microglia populations with transcriptional patterns similar to those of other CNS types such as astrocytes (cluster 7) or neurons (cluster 5). Thus, this novel method can generate organoids with physiologically relevant contents of microglia, astrocytes, neurons, and other brain cells, providing a platform to study interactions between CNS cell types in a 3D conformation.

CSF1 and IL34 are important proteins for the growth and maturation of microglia. The significantly induced expression of *CSF-1R*, a common receptor for both CSF-1 and IL34, in combination with the strong expression of *IL34* at the transcript level suggests a self-sufficient milieu for the survival and maturation of microglia in our CO-iM organoids. Furthermore, the significant induction of multiple sensome markers and general immunity-related transcripts by RNA-seq in CO-iMs is a compelling indication that microglia are functional in our organoid model. In addition, elevated levels of *C1q* and *C3*, the two main players involved in the initial activation of the complement cascade, along with *C3AR1, C7* and *MASP1*, suggest that microglia may play important roles in synapse pruning and refinement in our CO-iM model. Moreover, heightened complement activation could be detrimental and is associated with cognitive impairment because of excessive pruning [87–89]. CO-iMs downregulated some of their components, including *C4B* and *C5,* suggesting balanced regulation of pathways to maintain homeostatic conditions. Keeping in mind the high interest in developing targeted therapeutics against this pathway to mitigate neurodegeneration [90–93], we believe that CO-iMs could provide a good platform for high-throughput screening of small molecules and drugs that can specifically regulate complement activation. Overall, we can conclude that microglia in CO-iMs are functional because of their known immunity and particular susceptibility to HIV infection.

HIV enters the brain within two weeks of acute infection, and within the brain, microglia and macrophages are the major targets of HIV infection. In the post-cART era, it is imperative to understand and dissect the role of microglia in HIV neuropathogenesis to gain insights into two major unsolved issues, HAND and HIV latency. Several recent studies have shown that microglia are successfully infected with HIV, resulting in abrogated immune responses. Limitations of these studies include the use of monolayer cultures of microglia [55], the incorporation of externally infected microglia into maturing organoids [59], or the use of high amounts of virus particles to infect low-abundance microglia that develop innately in COs [56]. As microglia do not present the well-characterized SAMHD1 restriction to HIV-1 in myeloid cells (macrophage and dendritic cells [94]), we found them to be infected within 5 days of viral inoculation where the viruses were added to the culture media and crossed the organoid tissue layers to initiate replication deep into the organoids (Fig. 5J and K). We found that when CO-iMs with and without HIV infection were compared, there was a high upregulation of immune markers and their release with infection. We also compared inoculated CO-iMs with and without antiretrovirals that prevent the seeding of proviruses into the host genome and reported that the transcriptome related to immunity is dependent on viral replication. These findings allowed us to exclude the effect of extracellular/non-cytoplasmic immune responses such as TLR activation due to the presence of viruses in the inoculum. Interestingly, we find that not all microglia become infected despite the presence of high virus amounts in regions seeded with microglia, indicating a diversity of cells and a possible protective early triggering of innate responses and the cytokine milieu from the initial rounds of replication, which warrants further investigation. Infection of CO-iMs results in strong neuroinflammation profiles at both the transcriptomic (Fig. 5N and O) and cytokine levels (Fig. 5M), and infection results in a transcriptomic profile associated with the suppression of normal neural function and development

(Fig. 6). Despite controlling viral spread and systemic replication, modern antiretroviral therapies do not prevent any of the late stages of the HIV life cycle, as they focus on reverse transcriptase and integrase inhibitors, allowing for the production of nucleic acids, viral proteins, and viruses capable of maturation and fusion with other cells [36–39]. Thus, our model provides a unique platform to test specific molecular interactions between HIV particles and the cellular innate immune machinery that detects HIV and is known to mount cascades of immune responses. For example, innate sensing of foreign nucleic acids by cGAS/STING in blood myeloid cells occurs within the first hours of infection, followed by severe down regulation of their activation [95–97]. Although it was not the primary goal of this study, the observed robust infection of microglia in CO-iMs is highly encouraging to model patterns of HIV latency and viral rebound in the near future. Further, the control of HIV infection with ARVs shows that viral infection/replication can be controlled experimentally. Future applications of these organoid cultures would be to seed infection followed by blockage of replication by relevant ARVs at their concentrations measured in the brain to model the patterns of neuroinflammation resulting from a blockage of replication. It would be interesting to model the effect of cells that contain proviruses and still produce viral particles, despite control of replication (as current first line ART therapies do not block the late steps of the HIV life cycle) and how they modulate patterns of innate immunity (such as TLRs, cGAS/STING, MDA5/MAVS, etc.).

The CO-iM model offers a suitable platform where microglia with or without infection can crosstalk with other glial and neuronal cell types in a human-brain-like environment. As the cellular origin of CO-iMs is iPSCs, this platform is suitable for detailing mechanistic functions related to specific genes and to specific cellular lineages (HPCs vs NPCs), as iPSCs are easily genetically manipulated. In the context of HIV, this platform provides a unique opportunity to model the interaction of human microglia with their neuronal environment and renders it suitable for unmasking the role of microglia and their specific genes in virus-related inflammation, their role in HIV persistence under cART, and the biological consequences of infection for astrocytic and neuronal health.

Materials and methods

Culture and maintenance of iPSCs

Human iPSC lines were obtained from Rutgers University Cell and DNA Repository (RUCDR) Infinite Biologics (ID# NN0003920, source; male, fibroblast), termed iPSC-Ru and the Coriell Institute for Medical Research (Camden, NJ; ID#AG27602, source; female, fibroblast), termed iPSC-CRL, maintained in complete mTeSR + medium (Stem Cell Technologies; Vancouver, Canada) containing 0.1% penicillin/streptomycin and propagated as small aggregates via accutase or ReLeSR (Stem Cell Technologies). All iPSC colonies were cultured at 37 °C in a 5% CO_2 incubator on 6-well tissue culture plates coated with Matrigel (Corning, NY). The plates were coated by thoroughly mixing Matrigel thawed on ice with ice-cold DMEM/F-12 medium at a 1:100 dilution, followed by incubation at 1 ml/well for 1 h at room temperature or 37 °C in 5% CO_2. iPSCs were routinely validated for the markers OCT4, TRA-1–60 and Ki-67 via flow cytometry.

Labeling of iPSCs with TurboRFP and generation of HPCs

TurboRFP expressing lentiviral particles under the control of EF1a promoter (EF1A-RFP-LV) was purchased from Cellomics (Halethorpe, MD, # PLV-10072). iPSC-Ru were dissociated into single cells with accutase and plated at 0.3×10^6 cells per well of a 6-well plate in mTeSR +. Next day, cells were replaced with fresh mTeSR + and infected with EF1A-RFP-LV viral particles at 0.1 to 1.0 transduction units/cell. Three days later, wells were replaced with fresh mTeSR + media supplemented with puromycin (0.75 µg/ml). Media was changed every other day and healthy colonies formed under lowest viral concentrations were expanded for at least two more passages under puromycin (6–8 days per passage) before freezing the cells for stocking or differentiating into HPCs.

Both wild type (WT) and RFP labeled iPSCs were differentiated to HPCs using STEMdiff hematopoietic kit (Stem Cell Technologies). Briefly, iPSCs were dissociated into small colony clumps via ReLeSR treatment (incubating as per STEMCELL protocol, followed by minimal gentle pipetting) and plated at different dilutions of colonies per well of a 6-well plate in mTeSR +. On the next 24 to 48 h after confirming for optimal size and number of colonies (5–10 smal colonies/cm^2), mTSR + media was replaced with fresh media A and the protocol was followed for the next 12–14 days as per kit instructions (Stem Cell Technologies). On day 12 and day 14, round floating HPCs were harvested and cultured for up to three more days in X-vivo-15 basal media (Lonza, Switzerland), supplemented with 100 ng/mL M-CSF (Invitrogen, Massachusetts), 25 ng/mL IL-3 (R&D), 2 mM glutamax (Invitrogen), 0.055 mM β-mercaptoethanol (Invitrogen), 100 U/mL penicillin, and 100 µg/mL streptomycin. HPSCs phenotype was confirmed by flow cytometry before the cells were used for experiments or frozen for later usage. HPCs were routinely validated for expression of markers; CD45, CD43, and CD34 via flow cytometry.

Images of iPSC colonies and HPCs were captured under bright field or fluorescence using a Keyence

BZ-810 fluorescence microscope (Keyence, IL, USA) at 20× magnification. Cells were frozen in Cryo-SFM freezing media (Promo Cell, Heidelberg, Germany).

Generation of cerebral organoids

Cerebral organoids were generated using STEMdiff cerebral organoid kit (Stem Cell Technologies) with minor modifications. On day 0, iPSC colonies were suspended into single cells using accutase. To generate a regular CO, 10,000 iPSCs were incubated in organoid formation media; alternatively, to generate a CO-iM, 10,000 iPSCs were co-cultured with 3000 HPCs and incubated in organoid formation media. Ultra-low binding, round bottom 96-well plates (Corning) were used for embryoid body (EB) formation. Heat stable recombinant human bFGF (Gibco) at 5 U/ml was supplemented to organoid formation media only on day 0. In the case of CO-iMs, macrophage colony stimulating factor (MCSF, 50 ng/ml) and interleukin 3 (IL-3, 20 U/ml) were used throughout organoid development to support survival, proliferation and differentiation of HPCs to microglia. In order to prevent the fusion of multiple organoids during the maturation stage (around day 20), each organoid was separated into single wells in low binding 24-well plates with approximately 700 ml maturation media per organoid and incubated at 37 °C, 5% CO_2 on an orbital shaker at 90 rpm/min. Anti-adherent solution (Stem Cell Technologies) was used to create low binding plates. The figures represent organoids derived from iPSC-Ru, except when organoids derived from the iPSC-CRL line were used to demonstrate reproducibility. When so, this was clearly indicated in the respective legend section.

Single cell dissociation of organoids and flow cytometry

Organoids were gently washed with sterile HBSS, cut into small pieces, and incubated with papain (30 units/ml, Stem Cell Technologies) along with human recombinant DNAseI (20 U/ml, Roche) for 20–30 min at 37 °C, 5% CO_2 on an orbital shaker at 90 rpm/min. Preparation and activation of papain solution was performed as per the instructions (Stem Cell Technologies). One ml of papain solution per organoid per well in a 12-well plate was used. Approximately, every 10 min, organoids were dissociated by vigorous trituration (10 ~ 15 times) using a 1 mL pipette tip. By 30 min, most of the organoids dissociated into single cells and the remaining small tissue and cell aggregates were gently pressed using the back of a 1 ml syringe, and triturated. The whole cell suspension was passed through a cell strainer (40 µM) and washed with 2–3 ml of sterile HBSS. The flow through containing single cells were centrifuged at 1300 rpm for 8 min, washed again with sterile HBSS, resuspended in 1 ml HBSS, counted using a cell counter and processed for flow cytometry. This protocol consistently resulted in > 80% of cell viability as measured by trypan blue or calcein violet-AM (BioLegend).

iPSC colonies cultured on matrigel coated plates were detached with accutase and washed twice with sterile PBS. Floating HPCs were also washed twice with sterile PBS. Single cells from iPSC, HPCs or organoids were resuspended in 100 µl of PBS, incubated with Fc block (Cat #564,220, BD Biosciences, NJ) for 10 min at RT as per instructions and subjected to either cell surface staining for surface markers usingvia staining buffer (BD Biosciences), or intracellular staining using perm/fix reagents (BD Biosciences). For intracellular staining, cells were incubated with antibodies at 4 °C for 60 min in the dark, washed three times thoroughly with perm/wash buffer, resuspended in perm/wash buffer and run on a Fortessa flow cytometer (BD Biosciences). Primary conjugated antibodies used for flow are listed in supplementary Table 1. Data was analyzed using FlowJo software (v10.0.0) and normalized to the respective isotype IgGs or fluorescent minus one (FMOs) controls. For compensation, 2 drops of anti-mouse Ig, k beads (BD Biosciences) were incubated with primary antibodies for 20 min at 4 °C, washed once with PBS, then a drop of negative control BD comp beads (BD Biosciences) was added at the end and fixed with 2% paraformaldehyde. FlowJo was used to set compensation parameters.

RNA and DNA extraction from organoids

Organoids were stored in RNAlater (500 µl/organoid) at −20 °C until processing. RNA extraction was performed using the RNeasy mini kit (Qiagen, Hilden, Germany). Briefly, organoid was quickly brought to room temperature, RNA later was carefully removed and replaced with 500 µl of RLT lysis buffer in sterile tubes containing lysing matrix D beads (Cat #6,913,100, MP Biomedicals). Tubes were placed in a bead beater (BeadBlaster 24, Bechmark Scientific, NJ) at a speed of 4 M/S, for 30 s with 15 s intervals for 5 cycles to completely disintegrate and dissolve organoids in RLT buffer. Further steps were followed according to kit protocol. Column DNAse digestion was performed, and elution was done using only 40 µl of elution buffer. RNA was quantified using a nanodrop and samples that had 260/280 ratio of > 1.8 and 260/230 ratios between 2.0 and 2.2 were selected for further processing. Complementary DNA (cDNA) was synthesized using a Qscript kit (QuantaBio, MA) as per kit instructions in a T-100 (Bio-Rad) thermocycler.

For DNA extraction, organoids were removed from RNAlater, cut into small pieces and suspended in RLT buffer (700 µl/organoid) containing proteinase K. Samples were incubated at 56 °C for 30 min–2 h with intermittent vortexing until all the pieces were dissolved. Next

steps were followed according to DNAeasy Kit (Qiagen). DNA was eluted in 40 µl elution buffer and quantified using a nanodrop. Samples with 260/280 ratio of > 1.8 and 260/230 ratios between 2.0 and 2.2 were considered for further processing.

Quantitative real time PCR

Real time quantitative RT-PCR (RT-qPCR) was performed on cDNA samples (at least 1/20 volume) using SYBR green master mix. Samples were loaded on a 96-well fast block and run on a QuantStudio 5 Flex (Thermo Fisher) instrument. Protocol settings were as follows: hold stage (95 °C for 10 min), 45 cycles of PCR stage (95 °C for 20 s and 60 °C for 1 min) and melt curve stage (95 °C for 15 s, 60 °C for 1 min and 95 °C for 15 s). Primers used are listed in supplementary Table 2. Cycle threshold (Ct) values were subtracted with Ct values of housekeeping genes (GAPDH and 18S), relative expressions of genes were computed using $2^{-\Delta\Delta Ct}$ method and are expressed as fold changes compared to respective control groups.

Similarly, real time quantitative PCR (qPCR) was performed on DNA samples using Taqman based primers and probes for HIV DNA and human DNA essentially as previously described [98]. Ct values of HIV amplifications were normalized to human DNA and are expressed as fold changes compared to respective control groups.

HIV infection of cerebral organoids

Infectious particles of HIV-$1_{Ba\text{-}L}$ (Cat# ARP-510, BEI Resources) were produced in peripheral blood mononuclear cells (PBMCs) isolated from a healthy seronegative donor using Ficol-Hypaque density gradient centrifugation. Approximately 100 million cells were cultured in complete RPMI 1640 medium which included 10% heat-inactivated fetal bovine serum (Gemini Bio Products, Calabasas, CA), 2 mM L-glutamine (GlutaMAX supplement; ThermoFisher), 20 U/mL IL-2 (AIDS Reagent Program, Germantown, MD) and 1% penicillin/streptomycin (Sigma-Aldrich, St. Louis, MO), Cells were activated for 3 days with 1 µg/mL/million cells of purified NA/LE mouse anti-human CD3 and CD28 (BD Biosciences) and infected with HIV_{BaL} at 0.01 ng/10^6 cells. PBMCs were monitored to express at least 6–10% intracellular $p24^+$ in T lymphocytes before harvesting the supernatant. Supernatant was spun at 5000 rpm for 10 min to remove cell debris and concentrated via Lenti-X as per the instructions (Takara Bio). HIV-Gag-iGFP_JRFL (the following reagent was obtained through the NIH HIV Reagent Program, Division of AIDS, NIAID, NIH: Human Immunodeficiency Virus (HIV) Gag-iGFP_JRFL, ARP-12456, contributed by Dr. Benjamin Chen), containing an eGFP detailed in fused to GAG was produced and purified as previously [99, 100]. Purified viruses were quantified using a HIV1 p24 ELISA kit (#ab218268, Abcam, Waltham, MA). Approximately, 60 to70-day old organoids were infected with 7 ng of HIV p24 in low-binding 24 well plates at one organoid/well/700 µl of maturation media containing MCSF and IL-3. Three days later, the wells were gently washed and replaced with fresh maturation media. cART treatment consisted of plasma levels of nevirapine (NVP, 10 µM) and dolutegravir (DTG, 3.90 µg/mL) that were added 24 h prior to infection, at the time of infection, and after day 3 wash.

Immunofluorescence of organoids

Organoids were flash frozen fresh in cryomolds containing Tissue-Tek OCT (optimal cutting temperature) compound. Organoid specimens were washed twice in PBS and acclimated to OCT for few minutes in a small weight boat. Then, organoids were transferred into a labeled cryomold where they were oriented and fully immersed in OCT while avoiding bubble formation. The cryomolds containing the OCT immersed organoids were immediately transferred and submerged for about 10 s into a cooling bath consisting of a beaker containing 2-propanol inside a dry ice bucket until the OCT compound solidified or was visibly frozen. OCT blocks were kept on dry ice until stored at − 80 °C or sectioned (10–20 µm) into cover slips using a microtome cryostat and stored at − 80 °C.

Sections were subject to multiplex immunofluorescence (mIF) [101] staining for target cells and imaged by widefield deconvolution or spinning disk confocal microscopy mIF consisted of a series of consecutive rounds of staining and bleaching after initial fixing and blocking of tissues. Briefly, sections in cover slips were mounted and glued into home-made polyurethane resin staining chambers and fixed for 5 min at room temperature in the dark using a PIPES/PFA fixing solution (PIPES buffer pH 6.8, and 10% paraformaldehyde). After removing the fixing solution, tissues were washed three times with PBS and blocked for 1 h at room temperature using donkey serum blocking buffer (PBS, donkey serum, 10% sodium azide, and 10% triton X-100). All staining cocktails were prepared in blocking buffer and sections were stained for 1 h at room temperature or overnight at 4 °C. Additionally, bleaching was accomplished by exposing the tissues to light for 1 h at room temperature in bleaching buffer (7 volumes of distilled water, 2 volumes of 1 M $NaHCO_3$, and 1 volume of 30% H_2O_2). After removing the bleaching solution, tissues were washed three times with PBS and kept on PBS at 4 °C, or immediately used for a new round of staining. Antibodies used to stain COs are indicated and listed in supplementary Table S3. Ashlar (v1.18.0 https://github.com/labsyspharm/ashlar) was

used to align max intensity projection of the Z-stacks (0.5um spacing) for the multiple mIF rounds with max pixel deviation of 200 and filter sigma of 2.

Images were acquired with a Nikon wide-field Ti-e2 equipped with an LED light source (Spectra X) and a PCO edge 4.2BI camera using standard Chroma DAPI/GFP/TRITC/Cy5 polychroic and emission filters for DAPI/GFP/TRITC with oil 40× magnification or with a Nikon Ti-e2 spinning disk confocal (Crest X-Light V3) equipped with a celesta laser light source. Widefield images obtained with the widefield Nikon TIe-2 microscope were deconvolved with FlowDec using the Lucy-Richardson algorithm with the support of Pims relying on python 3.x using calculated PSFs from FlowDec as previously reported [95, 102].

Multiplex ELISA

Luminex assay for simultaneous quantification of multiple cytokines and chemokines (custom built, premixed kit) in the organoid supernatants were performed in a 96-well microplate format as per kit instructions (Lumsiinex performance assay, R & D Systems). Data capture was done using a Luminex Flexmap 3D analyzer (ThermoFisher) and data analysis used a five-parameter logistic (5-PL) curve fit of a standard curve per analyte.

Bulk RNA sequencing (RNAseq), single cell RNA sequencing (scRNAseq), and bioinformatics analysis

Total RNA was extracted from organoids using the RNeasy kit (Qiagen) and checked for concentration, RIN/RQN and 28S/18S ratios using Agilent 4150 TapeStation system (Agilent Technologies). Transcriptome sequencing was performed by DNBSEQ™ sequencing technology platform (BGI/Innomics) which includes stranded library preparation, 150 bp paired-end sequencing and ≥ 30million reads. Sequencing data was demultiplexed and trimmed using Trimmomatic v0.36 to remove adapters and low-quality reads. Trimmed reads were aligned to the Homo sapiens reference genome GRCh38 and transcripts quantified using the Hisat2-StringTie pipeline[58]. Differential gene expression analysis of the quantified gene transcripts was performed with DESeq2 v.1.42.0 R package using R v.4.3.2. After retaining genes with nonzero total read count, we identified differentially expressed genes (DEGs) either between CO-iMs and COs; HIV-infected and uninfected CO-iMs; or between ART-treated and untreated HIV-infected CO-iMs using as cut-offs an absolute log2 fold change > 1 and a false discovery rate (FDR) < 0.05 using the Benjamin-Hochberg procedure. Gene enrichment analyses for each comparison were subsequently performed using gene set enrichment analysis (GSEA) to identify specific Gene Ontologies (GO), KEGG, and REACTOME pathways associated with CO-iMs and/or HIV infection and ART treatment. We performed GSEA using clusterProfiler v.4.10.0 in R with all lists of genes ranked by the corresponding log2 fold change. For these analyses all genes whose gene symbols could be mapped to ENTREZ Ids using the org.Hs.eg.db v.3.18.0 Bioconductor annotation package were included.

For scRNAseq four CO-iMs were individually processed for isolation of single cells using papain and DNAse I treatment as previously described. The single cell suspensions from the organoids were resuspended in Parse cell buffer containing BSA, manually counted using a hemocytometer and assessed for cell viability by calcein violet-AM. The samples were centrifuged at 1,300 rpm for 10 min and then fixed/permeabilized using the Evercode fixation v2 kit (Parse Biosciences, ECF2101) and stored at − 80 °C according to the instructions. The bar-coding and library preparation for single cells were performed using the spit-pool based approach (Evercode™ WT Mini v2, Parse Biosciences). In brief, ~27,000 fixed cells from each organoid were pooled and underwent three rounds of barcoding. The final pooled cells were divided into 2 equal libraries for cDNA synthesis and library construction to recover 10,000 cells. Multiplexed libraries were sequenced using an Illumina NovaSeq X Plus system, with a 10B Flowcell and PE150 sequencing. Fastq files were generated from bcl files and processed using the 'Parse Biosciences analysis pipeline' using the GRCh38 reference genome to generate a gene expression matrix. After quality filtering, 6669 and 6331 estimated cells for each library were analyzed with 92,691 and 91,357 reads per cell, respectively. 40,666 and 40,588 genes were analyzed with a median of 4387 and 4279 genes per cell for each library. Seurat v.5.0.3 R package was used for analysis. We filtered cell barcodes with reads from less than 200 genes or more than 7500, as well as barcodes with more than 10% of mitochondrial genes that resulted in 11,440 remaining barcodes for analysis. We used the harmony method with 5000 variable features and 30 principal components to integrate the dataset from the two libraries and the Leiden method for clustering with 0.3 resolution using 10 principal components. To ensure robust clustering results, we tested a range of resolutions that extended from 0.1 to 1 (where smaller numbers lead to lower number of communities) and selected 0.3 as the most consistent result that did not provide a high number of clusters. Due to the small sample size, we aimed for the lower possible number of clusters that still provided a robust differentiation of the main cell types detected. DEGs that were upregulated in each cluster and expressed by a minimum of 25% of the cells in that cluster compared to the rest of the cells were identified using Seurat's implementation of the MAST

algorithm. Finally, ScType method R function using the default parameters and the curated ScType database filtered for brain tissue excluding cancer cells was used to annotate the clusters obtained. Cell types with at least 100 cells were considered by ScType for cluster annotation and the cell type with highest score per cluster was used as its most likely cell type. To fully disclose our analysis, we indicate both the assigned cell type as well as the other cell types considered in Fig. 4I. We confirmed the accuracy of the clusters by analyzing specific markers for the labels assigned to each cluster (Suppl. Figure 3).

Statistics

Statistical analyses were performed using Prism software (GraphPad Prism, San Diego, CA). Group comparisons were conducted using an unpaired, non-parametric Mann–Whitney test. Experiments were performed with multiple organoids and the data is presented with error bars as the standard error of the mean (SEM). The data in the figures represents single or different batches of CO or CO-iM, specific details for each case are detailed in the figure legends. A p-value of ≤ 0.05 was considered statistically significant, with * denoting $p \leq 0.05$, ** denoting $p \leq 0.01$, and *** denoting $p \leq 0.001$.

Supplementary Information

The online version contains supplementary material available at https://doi.org/10.1186/s12974-025-03353-2.

Supplementary materials 1. Figure 1: Quality assessment of iPSCs and HPCs. **A** Representative bright field image of iPSC-Ru. Scale bar, 100 µm. **B** Flow cytometry analysis (histogram) indicating iPSCs are positive for OCT-4, TRA-1–60 (pluripotency markers) and Ki67 (proliferation marker). **C** Representative bright field image of HPCs generated from iPSC-Ru. Scale bar, 100 µm. **D** Flow cytometry analysis (dot plot) of single cells from (C) indicating positivity for CD45, CD43 and CD34. **E** Cumulative data showing percent CD45/CD43, CD43/CD34 double positive as well as CD43 single positive cells in HPCs generated using iPSC-Ru line (n = 3 from the same batch). Data are presented as mean ± SEM. **F** Representative fluorescence image of iPSC-Ru expressing Turbo-RFP stably integrated via lentiviral approach. Scale bar, 100 µm. **G** Flow analysis (histogram) of single cells from (F) indicating RFP+ cells. **H** Representative fluorescence image of RFP+ HPCs generated from iPSC-Ru stably expressing Turbo-RFP. **I** Flow analysis (histogram) of single HPC cells from (H) indicating positivity for RFP.

Supplementary materials 2. Figure 2: Phenotypic characterization informing enrichment of microglia in CO-iMs. **A** Representative mIF image of a CO-iM stained for nucleus (Hoechst, white), microglia (Iba1, red), neurons (NeuN, green) and astrocytes (GFAP, blue). Scale bar, 250 µm (bottom right). Top panel showing individual staining for indicated markers and a merged image from all. **B** Zoomed in insets of i), ii) and iii) regions. Scale bars, 50 µm. **C** Representative mIF image of another CO-iM stained for nucleus (Hoechst, white), microglia (TMEM119, red), neurons (TUJ1, green), and astrocytes (GFAP, blue). Scale bar, 500 µm (left). Panel showing individual staining for indicated markers and a merged image from all. Scale bar, 500 µm (right). **D** mIF image of a CO-iM revealing microglia (TMEM119, red), astrocytes (GFAP, blue), and neurons (TUJ1, green) signals. Scale bar, 10 µm. **E, H** Representative dot plots showing S100β, GFAP, Nestin and Tuj1 positive populations from total cells in CO and CO-iMs, respectively. **I, J** Cumulative data indicating percent S100β, GFAP, Nestin and Tuj1 positive cells in CO and CO-iMs generated using iPSC-Ru line (n = 3–6 from a single batch). Each symbol represents an individual organoid. Data are presented as mean ± SEM using non-parametric Mann–Whitney test. *p < 0.05, **p < 0.01, ***p < 0.001. **K** A dot plot showing CD3+ population (T cells) in CO-iMs generated from iPSC-Ru line. Cyan and green dots represent isotype or CD3 antibody stained cells, respectively.

Supplementary materials 3. Figure 3: Genotypic characterization revealing enrichment of microglia markers in CO-iMs. RT-qPCR analysis of COs and CO-iMs (n = 5–7). mRNA levels were normalized to the endogenous reference *18S* and expressed as fold change relative to CO using the $2^{-(\Delta\Delta Ct)}$ method. Fold change for each sample was assessed by subtracting its ΔCt from average ΔCt, followed by $2^{-(\Delta\Delta Ct)}$. **A** mRNA levels of homeostatic microglia markers: *CD45*, *CD11B*, *IBA1* and *TMEM119* from one batch of COs and two batches of CO-iMs. **B** mRNA levels of NPC, astrocyte and mature neuronal markers as indicated in the text from respective single batches. **C, D** mRNA levels of *CD45*, *CD11B*, *IBA1* and *TMEM119* normalized to *GAPDH* or *18S* in COs (n = 5) and CO-iMs (n = 3) from respective single batches generated using iPSC-CRL. **E** mRNA levels of *S100β* and *Nestin* normalized to *GAPDH* or *18S* in COs (n = 5) and CO-iMs (n = 3) from respective single batches generated using iPSC-CRL. Each symbol represents an individual organoid. Data are presented as mean ± SEM using non-parametric Mann–Whitney test. *p < 0.05, **p < 0.01, ***p < 0.001. **F** Violin plots where single cell is represented by a dot showing relative expression levels for microglia representative transcript markers for each of the Seurat clusters displayed in Fig. 4. **G** Top 10 hits per Seurat clusters displayed in Fig. 4. **H** Violin plots where single cell is represented by a dot showing relative expression for astrocyte representative transcript markers for each of the Seurat cluster displayed in Fig. 4.

Supplementary materials 4. Figure 4: Microglia sensome and complement cascade pathway characterization in CO-iMs at mRNA level. RT-qPCR analysis of COs and CO-iMs to assess mRNA levels computed using the $2^{-(\Delta\Delta Ct)}$ method. Fold change for each sample in COs was assessed by subtracting its ΔCt from average ΔCt, followed by $2^{-(\Delta\Delta Ct)}$. **A** mRNA levels of microglia immune sensome markers: *CX3CR1*, *SLCO2B1*, *TLR4*, *CSF1-R* and *P2RY12* from iPSC-Ru line (n = 3 for CO from one batch, and n=10 for CO-iMs from two batches, and in the case of *P2RY12* n=5 for CO-iMs from one batch). **B, C** mRNA levels of *IL34,* an essential cytokine for microglia maturation and survival from iPSC-Ru line (n = 3 for CO and n=5 for CO-iM from one batch), and mRNA levels of *C3* and *C1Q*, components of complement pathway in CO and CO-iMs generated using iPSC-Ru. Ct values normalized to *18S*. **D** mRNA levels of *C3* and *C1Q*, in CO and CO-iMs generated using iPSC-CRL. Ct values normalized to *18S* or *GAPDH*. Each symbol represents an individual organoid. Data are presented as mean ± SEM using non-parametric Mann–Whitney test. *p < 0.05, **p < 0.01, ***p < 0.001.

Supplementary materials 5. Figure 5: Robust inflammatory response of CO-iMs generated from iPSC-Ru line to HIV-1 infection. **A** Immunofluorescence section image of two CO-iMs infected with HIV-iGFP-JRFL for 5 days Iba1+ (red), HIV+ (green), Hoescht (gray). Scale bars, 100µm. **B** CO-iMs were infected with HIV-iGFP_JRFL, mock infected or infected and treated with cART for 5 days as explained in the methods section, dissociated into single cell suspension and stained for cell surface microglia markers (CD45 and CD11b), and HIV (GFP) then analyzed via flow cytometry and plotted as a histogram. n = 1 for each group (mock, infected and infected +cART, respectively). **C** qPCR analysis for mRNA expression levels of various pro-inflammatory cytokines/chemokines (as indicated in the figure) in CO-iMs either infected with HIV_{BaL} for 5 days, or mock infected, or infected and treated with cART. n = 3 for uninfected and infected ± cART treated, and n = 3–4 for HIV infected CO-iMs from one batch. **D** A heatmap showing expression levels of a number of pro-inflammatory cytokines/chemokines in mock vs infected vs infected + cART treated CO-iMs. (n = 3 for each condition from one batch). Color indicates the expression level normalized for each gene using a Z-score. **E** RTqPCR analysis for mRNA expression levels of various pro-inflammatory cytokines/chemokines (as indicated in the figure) in CO-iMs either infected with HIV_{BaL} for 5 days, or mock infected, or infected and treated with cART. (n = 3 in each category). **F**

Volcano plot comparison of infected vs infected + cART treated CO-iMs indicating average log2 (fold change) versus -log10 (FDR) for all genes. Genes upregulated and downregulated by 2-fold change and FDR < 0.05 are labeled with red dots. Each symbol represents an individual organoid. Data are presented as mean ± SEM using non-parametric Mann–Whitney test. *p < 0.05, **p < 0.01, ***p < 0.001.

Supplementary materials 6.

Supplementary materials 7.

Supplementary materials 8.

Supplementary materials 9.

Acknowledgements
Library preparation and sequencing were performed at the Northwestern University NUSeq core. Cytokine panels were constructed by the Rush University Biomarker Development Core. We thank Dr. Muhammad Shoaib Arif for experimental insights on multiplex immunofluorescence.

Author contributions
JIM, SDN, JPZ and LA conceptualized and designed the study. SDN, JPZ, and JIM performed the study. All the authors interpreted the data. MKA contributed to the generation of the organoids and edited the manuscript. AR, JLAS, TS and SG helped with organoid slicing, imaging, RT–qPCR and p24 ELISA, respectively. CM provided assistance with the mIF initial set-up. RLR and JIM performed the RNA-seq and scRNA-seq analyses. SDN and JIM wrote the manuscript with input from all the authors.

Funding
This work was supported in part by grants from the NIH R01DA055497 and R01NS108796 to LA; the Walder Foundation innovation Top Up award to JRS; R01MH125778; P01AI169600; P30AI117943 Third Coast Center for AIDS Research (TC-CFAR) to RLR; and R21MH129205, R01MH139377 and R61DA058348 to JIM.

Data availability
Sequencing data generated in this study are available in the Gene Expression Omnibus (GEO) database under accession number GSE282644. For cerebral organoid samples processed for bulk RNAseq, GEO accession numbers are listed here for each sample type with the respective organoid numbers within parentheses as represented in Figs. 4D, H or 5O and supplementary Fig. 5D. GSM8648033, Uninfected_1 (CO-8); GSM8648034, Uninfected_2 (CO-9); GSM8648035, Uninfected_3 (CO-10); GSM8648036, Uninfected_4 (CO-iM-4); GSM8648037, Uninfected_5 (CO-iM-5); GSM8648038, Uninfected_6 (CO-iM-6); GSM8648039, HIV-1 BAL_1 (CO-iM-12); GSM8648040, HIV-1 BAL_2 (Co-iM-19); GSM8648041, HIV-1 BAL_3 (CO-iM-21); GSM8648042, HIV-1 BAL + cART_1 (CO-iM-15); GSM8648043, HIV-1 BAL + cART_2 (CO-iM-24); GSM8648044, HIV-1 BAL + cART_3 (CO-iM-25).

Declarations

Ethics approval and consent to participate
Not applicable.

Competing interests
The authors declare that they have no competing interests.

Received: 26 August 2024 Accepted: 23 January 2025
Published online: 10 February 2025

References

1. Mizee MR, Miedema SS, van der Poel M, Mizee, Schuurman KG, van Strien KG, et al. Isolation of primary microglia from the human post-mortem brain: effects of ante- and post-mortem variables. Acta Neuropathol Commun. 2017;5:16. https://doi.org/10.1186/s40478-017-0418-8.
2. Cochrane Catherine R, Angelovich Thomas A, Byrnes Sarah J, Waring E, Guanizo Aleks C, Trollope Gemma S, et al. Intact HIV proviruses persist in the brain despite viral suppression with ART. Ann Neurol. 2022;92:532–44. https://doi.org/10.1002/ana.26456.
3. Feng G, Jensen Frances E, Greely Henry T, Okano H, Treue S, Roberts Angela C, et al. Opportunities and limitations of genetically modified nonhuman primate models for neuroscience research. Proc Natl Acad Sci Pnas. 2020;117:24022–31. https://doi.org/10.1073/pnas.2006515117.
4. Jennings CG, Landman R, Zhou Y, Sharma J, Hyman J, Movshon JA, et al. Opportunities and challenges in modeling human brain disorders in transgenic primates. Nat Neurosci. 2016;19:1123–30.
5. Agarwal Y, Beatty C, Biradar S, Castronova I, Ho S, Melody K, et al. Moving beyond the mousetrap: current and emerging humanized mouse and rat models for investigating prevention and cure strategies against HIV infection and associated pathologies. Retrovirology. 2020;17:8. https://doi.org/10.1186/s12977-020-00515-3.
6. Urbach YK, Bode FJ, Nguyen HP, Riess O, Von Hörsten S. Neurobehavioral Tests in Rat Models of Degenerative Brain Diseases. In: Anegon I, editor. Rat Genomics. Totowa, NJ: Humana Press; 2010 p. 333–56. https://doi.org/10.1007/978-1-60327-389-3_24
7. Pauletti A, Terrone G, Shekh-Ahmad T, Salamone A, Ravizza T, Rizzi M, et al. Targeting oxidative stress improves disease outcomes in a rat model of acquired epilepsy. Brain. 2019;142:e39–e39.
8. Gage FH, Temple S. Neural stem cells: generating and regenerating the brain. Neuron. 2013;80:588–601.
9. Manghera M, Ferguson J, Douville R. ERVK polyprotein processing and reverse transcriptase expression in human cell line models of neurological disease. Viruses. 2015;7:320–32.
10. Dello Russo C, Cappoli N, Coletta I, Mezzogori D, Paciello F, Pozzoli G, et al. The human microglial HMC3 cell line: where do we stand? A systematic literature review. J Neuroinflammat. 2018;15:259. https://doi.org/10.1186/s12974-018-1288-0.
11. Chai Q, Jovasevic V, Malikov V, Sabo Y, Morham S, Walsh D, et al. HIV-1 counteracts an innate restriction by amyloid precursor protein resulting in neurodegeneration. Nat Commun. 2017;8:1522.
12. Chai Q, Jovasevic V, Malikov V, Sabo Y, Morham S, Walsh D, et al. Author Correction: HIV-1 counteracts an innate restriction by amyloid precursor protein resulting in neurodegeneration. Nat Commun. 2018;9:2257.
13. Dezonne RS, Sartore RC, Nascimento JM, Saia-Cereda VM, Romão LF, Alves-Leon SV, et al. Derivation of functional human astrocytes from cerebral organoids. Sci Rep. 2017;7:45091.
14. Sun N, Meng X, Liu Y, Song D, Jiang C, Cai J. Applications of brain organoids in neurodevelopment and neurological diseases. J Biomed Sci. 2021;28:30. https://doi.org/10.1186/s12929-021-00728-4.
15. Eichmüller OL, Knoblich JA. Human cerebral organoids—a new tool for clinical neurology research. Nat Rev Neurol. 2022;18:661–80.
16. Lancaster MA, Renner M, Martin C-A, Wenzel D, Bicknell LS, Hurles ME, et al. Cerebral organoids model human brain development and microcephaly. Nature. 2013;501:373–9.
17. Subramanian L, Bershteyn M, Paredes MF, Kriegstein AR. Dynamic behaviour of human neuroepithelial cells in the developing forebrain. Nat Commun. 2017;8:14167.
18. Velasco S, Kedaigle AJ, Simmons SK, Nash A, Rocha M, Quadrato G, et al. Individual brain organoids reproducibly form cell diversity of the human cerebral cortex. Nature. 2019;570:523–7.
19. Di Lullo E, Kriegstein AR. The use of brain organoids to investigate neural development and disease. Nat Rev Neurosci. 2017;18:573–84.
20. Hopkins HK, Traverse EM, Barr KL. Methodologies for generating brain organoids to model viral pathogenesis in the CNS. Pathogens. 2021;10:1510.
21. Camp JG, Badsha F, Florio M, Kanton S, Gerber T, Wilsch-Bräuninger M, et al. Human cerebral organoids recapitulate gene expression programs of fetal neocortex development. Proc Natl Acad Sci. 2015;112:15672–7. https://doi.org/10.1073/pnas.1520760112.
22. Quadrato G, Nguyen T, Macosko EZ, Sherwood JL, Min Yang S, Berger DR, et al. Cell diversity and network dynamics in photosensitive human brain organoids. Nature. 2017;545:48–53.

23. Mansour AA, Schafer ST, Gage FH. Cellular complexity in brain organoids: current progress and unsolved issues. Semin Cell Dev Biol. 2021;111:32–9.
24. Qian X, Nguyen HN, Song MM, Hadiono C, Ogden SC, Hammack C, et al. Brain-region-specific organoids using mini-bioreactors for modeling ZIKV exposure. Cell. 2016;165:1238–54.
25. Muffat J, Li Y, Yuan B, Mitalipova M, Omer A, Corcoran S, et al. Efficient derivation of microglia-like cells from human pluripotent stem cells. Nat Med. 2016;22:1358–67.
26. Abreu CM, Gama L, Krasemann S, Chesnut M, Odwin-Dacosta S, Hogberg HT, et al. Microglia increase inflammatory responses in iPSC-derived human brainspheres. Front Microbiol. 2018. https://doi.org/10.3389/fmicb.2018.02766.
27. Lin Y-T, Seo J, Gao F, Feldman HM, Wen H-L, Penney J, et al. APOE4 causes widespread molecular and cellular alterations associated with Alzheimer's disease phenotypes in human iPSC-derived brain cell types. Neuron. 2018;98:1141-1154.e7.
28. Valcour V, Chalermchai T, Sailasuta N, Marovich M, Lerdlum S, Suttichom D, et al. Central nervous system viral invasion and inflammation during acute HIV infection. J Infect Dis. 2012;206:275–82.
29. Liu J, Ghneim K, Sok D, Bosche William J, Li Y, Chipriano E, et al. Antibody-mediated protection against SHIV challenge includes systemic clearance of distal virus. Sci AAAS. 2016;353:1045–9. https://doi.org/10.1126/science.aag0491.
30. Deeks SG, Overbaugh J, Phillips A, Buchbinder S. HIV infection. Nat Rev Dis Primer. 2015;1:15035.
31. Wang Y, Liu M, Lu Q, Farrell M, Lappin JM, Shi J, et al. Global prevalence and burden of HIV-associated neurocognitive disorder: a meta-analysis. Neurology. 2020;95:e2610–21. https://doi.org/10.1212/WNL.0000000000010752.
32. Zhou L, Saksena NK. HIV associated neurocognitive disorders. Infect Dis Rep. 2013;5: e8.
33. Lorenzo-Redondo R, Fryer Helen R, Bedford T, Kim E-Y, Archer J, Kosakovsky Pond Sergei L, et al. Persistent HIV-1 replication maintains the tissue reservoir during therapy. Nature. 2016;530:51–6. https://doi.org/10.1038/nature16933.
34. Spudich S, Robertson KR, Bosch RJ, Gandhi RT, Cyktor JC, Mar H, et al. Persistent HIV-infected cells in cerebrospinal fluid are associated with poorer neurocognitive performance. J Clin Invest. 2019;129:3339–46.
35. Gisolf EH, van Praag RME, Jurriaans S, Portegies P, Goudsmit J, Danner SA, et al. Increasing cerebrospinal fluid chemokine concentrations despite undetectable cerebrospinal fluid HIV RNA in HIV-1-infected patients receiving antiretroviral therapy. JAIDS J Acquir Immune Defic Syndr. 2000;25:426.
36. Pollack RA, Jones RB, Pertea M, Bruner KM, Martin AR, Thomas AS, et al. Defective HIV-1 proviruses are expressed and can be recognized by cytotoxic T lymphocytes which shapes the proviral landscape. Cell Host Microbe. 2017;21:494-506.e4.
37. Klatt NR, Chomont N, Douek DC, Deeks SG. Immune activation and HIV persistence: implications for curative approaches to HIV infection. Immunol Rev. 2013;254:326–42.
38. Imamichi H, Dewar RL, Adelsberger JW, Rehm CA, O'Doherty U, Paxinos EE, et al. Defective HIV-1 proviruses produce novel protein-coding RNA species in HIV-infected patients on combination antiretroviral therapy. Proc Natl Acad Sci U S A. 2016;113:8783–8.
39. Mohammadzadeh N, Roda W, Branton WG, Clain J, Rabezanahary H, Zghidi-Abouzid O, et al. Lentiviral infections persist in brain despite effective antiretroviral therapy and neuroimmune activation. MBio. 2021;12:e0278421.
40. Fauci A, Desrosiers R. Pathogenesis of HIV and SI. 1997; 9.
41. Post K, Olson ED, Naufer MN, Gorelick RJ, Rouzina I, Williams MC, et al. Mechanistic differences between HIV-1 and SIV nucleocapsid proteins and cross-species HIV-1 genomic RNA recognition. Retrovirology. 2016;13:89. https://doi.org/10.1186/s12977-016-0322-5.
42. Zhang J, Diehl GE, Littman DR. Relief of preintegration inhibition and characterization of additional blocks for HIV replication in primary mouse T cells. KewalRamani VN, editor. PLoS ONE. 2008;3:e2035. https://doi.org/10.1371/journal.pone.0002035.
43. Greenblatt MB, Vbranac V, Tivey T, Tsang K, Tager AM, Aliprantis AO. Graft versus host disease in the bone marrow, liver and thymus humanized mouse model. PLoS ONE. 2012;7: e44664. https://doi.org/10.1371/journal.pone.0044664.
44. Shultz LD, Ishikawa F, Greiner DL. Humanized mice in translational biomedical research. Nat Rev Immunol. 2007;7:118–30.
45. Wallet C, De Rovere M, Van Assche J, Daouad F, De Wit S, Gautier V, et al. Microglial cells: the main HIV-1 reservoir in the brain. Front Cell Infect Microbiol. 2019. https://doi.org/10.3389/fcimb.2019.00362.
46. Ash MK, Al-Harthi L, Schneider JR. HIV in the brain: identifying viral reservoirs and addressing the challenges of an HIV cure. Vaccines. 2021;9:867.
47. Churchill MJ, Gorry PR, Cowley D, Lal L, Sonza S, Purcell DFJ, et al. Use of laser capture microdissection to detect integrated HIV-1 DNA in macrophages and astrocytes from autopsy brain tissues. J Neurovirol. 2006;12:146–52.
48. Trillo-Pazos G, Diamanturos A, Rislove L, Menza T, Chao W, Belem P, et al. Detection of HIV-1 DNA in microglia/macrophages, astrocytes and neurons isolated from brain tissue with HIV-1 encephalitis by laser capture microdissection. Brain Pathol Zurich Switz. 2003;13:144–54.
49. Narasipura SD, Kim S, Al-Harthi L. Epigenetic regulation of HIV-1 latency in astrocytes. J Virol. 2014;88:3031–8. https://doi.org/10.1128/jvi.03333-13.
50. Narasipura SD, Henderson LJ, Fu SW, Chen L, Kashanchi F, Al-Harthi L. Role of β-catenin and TCF/LEF family members in transcriptional activity of HIV in astrocytes. J Virol. 2012;86:1911–21. https://doi.org/10.1128/JVI.06266-11.
51. Lamers SL, Rose R, Maidji E, Agsalda-Garcia M, Nolan DJ, Fogel GB, et al. HIV DNA is frequently present within pathologic tissues evaluated at autopsy from combined antiretroviral therapy-treated patients with undetectable viral loads. Kirchhoff F, editor. J Virol. 2016;90:8968–83.
52. Fischer-Smith T, Tedaldi EM, Rappaport J. CD163/CD16 coexpression by circulating monocytes/macrophages in HIV: potential biomarkers for HIV infection and AIDS progression. AIDS Res Hum Retroviruses. 2008;24:417–21. https://doi.org/10.1089/aid.2007.0193.
53. Koppensteiner H, Brack-Werner R, Schindler M. Macrophages and their relevance in human immunodeficiency virus type I infection. Retrovirology. 2012;9:82. https://doi.org/10.1186/1742-4690-9-82.
54. Lutgen V, Narasipura SD, Barbian HJ, Richards M, Wallace J, Razmpour R, et al. HIV infects astrocytes in vivo and egresses from the brain to the periphery. PLoS Pathog. 2020;16: e1008381.
55. Tang Y, Chaillon A, Gianella S, Wong LM, Li D, Simermeyer TL, et al. Brain microglia serve as a persistent HIV reservoir despite durable antiretroviral therapy. J Clin Invest. 2022;133: e167417.
56. Ormel PR, Vieira de Sá R, van Bodegraven EJ, Karst H, Harschnitz O, Sneeboer MAM, et al. Microglia innately develop within cerebral organoids. Nat Commun. 2018;9:4167.
57. Donadoni M, Cakir S, Bellizzi A, Swingler M, Sariyer IK. Modeling HIV-1 infection and NeuroHIV in hiPSCs-derived cerebral organoid cultures. J Neurovirol. 2024. https://doi.org/10.1007/s13365-024-01204-z.
58. Gumbs S, Kübler R, Gharu L, Schipper P, Borst A, Snijders G, et al. Human microglial models to study HIV infection and neuropathogenesis: a literature overview and comparative analyses. J Neurovirol. 2022;28(1):64–91.
59. dos Reis RS, Sant S, Keeney H, Wagner MCE, Ayyavoo V. Modeling HIV-1 neuropathogenesis using three-dimensional human brain organoids (hBORGs) with HIV-1 infected microglia. Sci Rep. 2020;10:15209.
60. Cakir B, Tanaka Y, Kiral FR, Xiang Y, Dagliyan O, Wang J, et al. Expression of the transcription factor PU.1 induces the generation of microglia-like cells in human cortical organoids. Nat Commun. 2022;13:430.
61. Xu R, Boreland AJ, Li X, Erickson C, Jin M, Atkins C, et al. Developing human pluripotent stem cell-based cerebral organoids with a controllable microglia ratio for modeling brain development and pathology. Stem Cell Rep. 2021;16:1923–37.
62. Jin M, Xu R, Wang L, Alam M, Ma Z, Zhu S, et al. Type-I-interferon signaling drives microglial dysfunction and senescence in human iPSC models of down syndrome and Alzheimer's disease. Cell Stem Cell. 2022;29:1135-1153.E8.
63. Schafer ST, Mansour AA, Schlachetzki JCM, Pena M, Ghassemzadeh S, Mitchell L, et al. An in vivo neuroimmune organoid model to study human microglia phenotypes. Cell. 2023;186:2111-2126.e20.

64. McQuade A, Coburn M, Tu CH, Hasselmann J, Davtyan H, Blurton-Jones M. Development and validation of a simplified method to generate human microglia from pluripotent stem cells. Mol Neurodegener. 2018;13:67. https://doi.org/10.1186/s13024-018-0297-x.
65. Abud EM, Ramirez RN, Martinez ES, Healy LM, Nguyen CHH, Newman SA, et al. iPSC-derived human microglia-like cells to study neurological diseases. Neuron. 2017;94:278-293.e9.
66. Jurga AM, Paleczna M, Kuter KZ. Overview of general and discriminating markers of differential microglia phenotypes. Front Cell Neurosci. 2020. https://doi.org/10.3389/fncel.2020.00198.
67. Greter M, Merad M. Regulation of microglia development and homeostasis. Glia. 2013;61:121–7. https://doi.org/10.1002/glia.22408.
68. Ford AL, Goodsall AL, Hickey WF, Sedgwick JD. Normal adult ramified microglia separated from other central nervous system macrophages by flow cytometric sorting. Phenotypic differences defined and direct ex vivo antigen presentation to myelin basic protein-reactive CD4+ T cells compared. J Immunol Baltim Md. 1995;154:4309–21.
69. Hernández D, Rooney LA, Daniszewski M, Gulluyan L, Liang HH, Cook AL, et al. Culture variabilities of human iPSC-derived cerebral organoids are a major issue for the modelling of phenotypes observed in Alzheimer's disease. Stem Cell Rev Rep. 2022;18:718–31. https://doi.org/10.1007/s12015-021-10147-5.
70. Ball JB, Green-Fulgham SM, Watkins LR. Mechanisms of microglia-mediated synapse turnover and synaptogenesis. Prog Neurobiol. 2022;218:102336.
71. Hickman SE, El Khoury J. Analysis of the microglial sensome. Methods Mol Biol Clifton NJ. 2019;2034:305–23.
72. Hickman SE, Kingery ND, Ohsumi TK, Borowsky ML, Wang L, Means TK, et al. The microglial sensome revealed by direct RNA sequencing. Nat Neurosci. 2013;16:1896–905.
73. Stevens B, Allen NJ, Vazquez LE, Howell GR, Christopherson KS, Nouri N, et al. The classical complement cascade mediates CNS synapse elimination. Cell. 2007;131:1164–78.
74. Brown RM, Rana PSJB, Jaeger HK, O'Dowd JM, Balemba OB, Fortunato EA. Human cytomegalovirus compromises development of cerebral organoids. J Virol. 2019;93:e00957-e1019.
75. Hübner W, Chen P, Portillo AD, Liu Y, Gordon RE, Chen BK. Sequence of human immunodeficiency virus type 1 (HIV-1) gag localization and oligomerization monitored with live confocal imaging of a replication-competent, fluorescently tagged HIV-1. J Virol. 2007;81:12596–607. https://doi.org/10.1128/JVI.01088-07.
76. Dang J, Tiwari SK, Lichinchi G, Qin Y, Patil VS, Eroshkin AM, et al. Zika virus depletes neural progenitors in human cerebral organoids through activation of the innate immune receptor TLR3. Cell Stem Cell. 2016;19:258–65.
77. Watanabe M, Buth JE, Vishlaghi N, de la Torre-Ubieta L, Taxidis J, Khakh BS, et al. Self-organized cerebral organoids with human-specific features predict effective drugs to combat zika virus infection. Cell Rep. 2017;21:517–32.
78. Lier J, Streit WJ, Bechmann I. Beyond activation: characterizing microglial functional phenotypes. Cells. 2021;10:2236.
79. De Rivero Vaccari JP, Lotocki G, Marcillo AE, Dietrich WD, Keane RW. A molecular platform in neurons regulates inflammation after spinal cord injury. J Neurosci. 2008;28:3404–14. https://doi.org/10.1523/JNEUROSCI.0157-08.2008.
80. Espinosa-Oliva AM, García-Revilla J, Alonso-Bellido IM, Burguillos MA. Brainiac caspases: beyond the wall of apoptosis. Front Cell Neurosci. 2019;13:500. https://doi.org/10.3389/fncel.2019.00500/full.
81. Lin W-P, Xiong G-P, Lin Q, Chen X-W, Zhang L-Q, Shi J-X, et al. Heme oxygenase-1 promotes neuron survival through down-regulation of neuronal NLRP1 expression after spinal cord injury. J Neuroinflammat. 2016;13:52.
82. McInnis JJ, Sood D, Guo L, Dufault MR, Garcia M, Passaro R, et al. Unravelling neuronal and glial differences in ceramide composition, synthesis, and sensitivity to toxicity. Communicat Bio. 2023. https://doi.org/10.1101/2023.12.06.569570.
83. Elkjaer ML, Hartebrodt A, Oubounyt M, Weber A, Vitved L, Reynolds R, et al. Single-cell multi-omics map of cell type-specific mechanistic drivers of multiple sclerosis lesions. Neurol Neuroimmunol Neuroinflammation. 2024;11: e200213. https://doi.org/10.1212/NXI.0000000000200213.
84. Frost JL, Schafer DP. Microglia: architects of the developing nervous system. Trends Cell Biol. 2016;26:587–97.
85. Herculano-Houzel S. The glia/neuron ratio: how it varies uniformly across brain structures and species and what that means for brain physiology and evolution. Glia. 2014;62:1377–91.
86. Amadio S, Parisi C, Montilli C, Carrubba AS, Apolloni S, Volonté C. $P2Y_{12}$ receptor on the verge of a neuroinflammatory breakdown. Mediators Inflamm. 2014;2014:1–15.
87. Hong S, Beja-Glasser VF, Nfonoyim BM, Frouin A, Li S, Ramakrishnan S, et al. Complement and microglia mediate early synapse loss in Alzheimer mouse models. Science. 2016;352:712–6.
88. Markarian M, Krattli RP, Baddour JD, Alikhani L, Giedzinski E, Usmani MT, et al. Glia-selective deletion of complement C1q prevents radiation-induced cognitive deficits and neuroinflammation. Cancer Res. 2021;81:1732–44.
89. Vasek MJ, Garber C, Dorsey D, Durrant DM, Bollman B, Soung A, et al. A complement-microglial axis drives synapse loss during virus-induced memory impairment. Nature. 2016;534:538–43.
90. Gavriilaki M, Kimiskidis VK, Gavriilaki E. Precision medicine in neurology: the inspirational paradigm of complement therapeutics. Pharmaceuticals. 2020;13:341.
91. Garred P, Tenner AJ, Mollnes TE. Therapeutic targeting of the complement system: from rare diseases to pandemics. Levy FO, editor. Pharmacol Rev. 2021;73:792–827.
92. Mastellos DC, Ricklin D, Lambris JD. Clinical promise of next-generation complement therapeutics. Nat Rev Drug Discov. 2019;18:707–29.
93. Zelek WM, Xie L, Morgan BP, Harris CL. Compendium of current complement therapeutics. Mol Immunol. 2019;114:341–52.
94. Cenker JJ, Stultz RD, McDonald D. Brain microglial cells are highly susceptible to HIV-1 infection and spread. AIDS Res Hum Retrovirus. 2017;33:1155–65. https://doi.org/10.1089/aid.2017.0004.
95. Yoh SM, Mamede JI, Lau D, Ahn N, Sánchez-Aparicio MT, Temple J, et al. Recognition of HIV-1 capsid by PQBP1 licenses an innate immune sensing of nascent HIV-1 DNA. Mol Cell. 2022;82:2871-2884.e6.
96. Gao D, Wu J, Wu Y-T, Du F, Aroh C, Yan N, et al. Cyclic GMP-AMP synthase is an innate immune sensor of HIV and other retroviruses. Science. 2013;341:903–6. https://doi.org/10.1126/science.1240933.
97. Wang P-H, Fung S-Y, Gao W-W, Deng J-J, Cheng Y, Chaudhary V, et al. A novel transcript isoform of STING that sequesters cGAMP and dominantly inhibits innate nucleic acid sensing. Nucleic Acids Res. 2018;46:4054–71.
98. Albalawi YA, Narasipura SD, Olivares LJ, Al-Harthi L. CD4dim CD8bright T cells home to the brain and mediate HIV neuroinvasion. J Virol. 2022;96:e00804-e822. https://doi.org/10.1128/jvi.00804-22.
99. Mamede JI, Hope TJ. Detection and tracking of dual-labeled HIV particles using wide-field live cell imaging to follow viral core integrity. HIV Protoc. 2016. https://doi.org/10.1007/978-1-4939-3046-3_4.
100. Mamede JI, Cianci GC, Anderson MR, Hope TJ. Early cytoplasmic uncoating is associated with infectivity of HIV-1. Proc Natl Acad Sci USA. 2017;114:E7169–78.
101. Tan WCC, Nerurkar SN, Cai HY, Ng HHM, Wu D, Wee YTF, et al. Overview of multiplex immunohistochemistry/immunofluorescence techniques in the era of cancer immunotherapy. Cancer Commun. 2020;40:135–53. https://doi.org/10.1002/cac2.12023.
102. Carter SD, Mamede JI, Hope TJ, Jensen GJ. Correlated cryogenic fluorescence microscopy and electron cryo-tomography shows that exogenous TRIM5α can form hexagonal lattices or autophagy aggregates in vivo. Proc Natl Acad Sci. 2020;117:29702–11.

Publisher's Note